

# qHEOM: A Quantum Algorithm for Simulating Non-Markovian Quantum Dynamics Using the Hierarchical Equations of Motion

Xiaohan Dan,<sup>†</sup> Eitan Geva,<sup>‡</sup> and Victor S. Batista<sup>\*,†,¶</sup>

<sup>†</sup>*Department of Chemistry, Yale University, New Haven, CT 06520, USA*

<sup>‡</sup>*Department of Chemistry, University of Michigan, Ann Arbor, MI 48109, USA*

<sup>¶</sup>*Yale Quantum Institute, Yale University, New Haven, CT 06511, USA*

E-mail: victor.batista@yale.edu

## Abstract

Quantum computing offers promising new avenues for tackling the long-standing challenge of simulating the quantum dynamics of complex chemical systems, particularly open quantum systems coupled to external baths. However, simulating such non-unitary dynamics on quantum computers is challenging since quantum circuits are specifically designed to carry out unitary transformations. Furthermore, chemical systems are often strongly coupled to the surrounding environment, rendering the dynamics non-Markovian and beyond the scope of Markovian quantum master equations like Lindblad or Redfield. In this work, we introduce a quantum algorithm designed to simulate non-Markovian dynamics of open quantum systems. Our approach enables the implementation of arbitrary quantum master equations on noisy intermediate-scale quantum (NISQ) computers. We illustrate the method as applied in conjunction with the numerically exact hierarchical equations of motion (HEOM) method. The effectiveness of the resulting quantum HEOM algorithm (qHEOM) is demonstrated as applied

to simulations of the non-Lindbladian electronic energy and charge transfer dynamics in models of the carotenoid-porphyrin-C<sub>60</sub> molecular triad dissolved in tetrahydrofuran and the Fenna-Matthews-Olson complex.

# 1 Introduction

Simulations of open quantum systems are essential for theoretical studies of a wide range of chemical processes, including charge transfer, energy transfer, and proton transfer in solutions or biological systems.<sup>1-3</sup> However, accurate simulations of such systems are challenging and often rely on the Markovian approximation. Here, we introduce a quantum algorithm for simulations of non-Markovian open quantum systems on noisy intermediate-scale quantum (NISQ) computers.

Traditionally, dynamical simulations of open quantum systems relied on Markovian quantum master equations of the Redfield or Lindblad types. These approaches assume that the system is weakly coupled to a bath so that the coupling can be treated within second-order perturbation theory.<sup>2,4-9</sup> While effective in numerous scenarios, these methods fall short when chemical systems exhibit non-Markovian behavior. This occurs under conditions such as strong system-environment coupling, low temperatures, structured or finite reservoirs, or initial correlations between the system and its environment.<sup>10-14</sup>

To address non-Markovian dynamics, various non-perturbative methods have been developed, including tensor train thermo-field dynamics (TT-TFD),<sup>15-18</sup> the hierarchical equations of motion (HEOM),<sup>14,19-24</sup> the multilayer multiconfiguration time-dependent Hartree (ML-MCTDH),<sup>25,26</sup> path integral techniques,<sup>27-35</sup> and the generalized quantum master equation (GQME).<sup>13,17,36-47</sup>

Recent advancements in quantum computing hardware have opened new possibilities for simulating quantum dynamics on quantum computers.<sup>48-52</sup> Most quantum algorithms have focused on closed systems, where unitary dynamics can be directly mapped onto quantum circuits.<sup>52-54</sup> However, the inherently non-unitary nature of open quantum systems dynamics

presents a unique challenge for quantum computing, as quantum circuits are specifically designed to implement unitary transformations.<sup>48,55,56</sup>

Efforts to bridge this gap and map non-unitary dynamics into a unitary framework have led to the development of the linear combination of unitaries (LCU),<sup>57–59</sup> dilation methods,<sup>55,56,60–62</sup> imaginary time evolution,<sup>63–65</sup> and variational quantum algorithms.<sup>66–69</sup> However, most quantum algorithms are tailored to systems governed by the Lindblad quantum master equation, which assumes weak system-bath coupling and Markovian dynamics. While these algorithms have been applied to simulate relatively simple models, such as spontaneous emission and two-level systems,<sup>56–58,61,65,70–72</sup> their application to more complex model systems like the transverse field Ising model,<sup>58,65,68,72</sup> and the Fenna-Matthews-Olson (FMO) complex,<sup>73</sup> often relies on ad-hoc choices of Lindblad operators, which may not fully capture dephasing or damping processes induced by the environment.

In this work, we introduce the quantum HEOM algorithm (qHEOM) by implementing the numerically exact HEOM approach with the dilation method to simulate non-Markovian dynamics in open quantum systems. We illustrate the capabilities of the qHEOM algorithm on IBM quantum computers as applied to simulations of charge transfer dynamics in a solvated molecular triad<sup>74</sup> and electronic energy transfer dynamics in the FMO complex. Additionally, we assess the applicability of the commonly used Lindblad equation derived from the microscopic Hamiltonians of the model systems of interest. By comparing the results obtained by integrating the Lindblad equation with those obtained from the qHEOM method, we illustrate the limitations of the Lindblad equation across the parameter regimes relevant to electronic charge and energy transfer processes.

Our qHEOM method belongs to the family of recently proposed quantum algorithms for non-Markovian evolution.<sup>34,35,59,60,62,75</sup> Using the Sz.-Nagy dilation theorem,<sup>76</sup> Wang *et al.*<sup>62</sup> dilated the propagator obtained from the GQME. Walters *et al.*<sup>34</sup> constructed the propagator time series that spans a memory time using the path integral approach, and dilated it into unitary gates. Seneviratne *et al.*<sup>35</sup> used dilation based on singular value

decomposition<sup>61</sup> (SVD dilation) to dilate the Kraus operators that are calculated through path integral. Li *et al.*<sup>59</sup> presented a quantum algorithm based on the linear combination of unitaries (LCU) approach<sup>58</sup> to implement the numerically exact dissipaton-embedded quantum master equation in second quantization (DQME-SQ).

The qHEOM algorithm offers several key advantages over the methods mentioned above. First, it employs the SVD dilation methodology that can be applied to dilate propagators from a wide range of master equations. This SVD approach essentially decomposes the propagator into a sum of two unitary operators that require much fewer shots than the traditional LCU method based on the Taylor expansion.<sup>58</sup> Second, when compared to Sz.-Nagy dilation, the SVD approach dilates only the diagonal matrix of singular values, significantly reducing the circuit depth. Additionally, the diagonal unitary operator of singular values can be efficiently implemented using the Walsh operator representation,<sup>77</sup> further reducing circuit complexity. Another important advantage of qHEOM is that it employs projection operators to map vectors from the HEOM space to the state vector for quantum computing. The flexibility in choosing the projection subspace allows us to select a smaller subspace and reduce the dimension of the propagator, thereby decreasing the number of qubits and circuit complexity on NISQ devices.

The outline of this paper is as follows. Section 2 introduces our quantum algorithm for the propagation of non-Markovian dynamics based on SVD dilation. Section 3 describes the simulation methods based on the HEOM and Lindblad equations. Section 4 presents the model systems used for electronic charge and energy transfer simulations. Section 5 compares the simulation results from HEOM and the Lindblad equation on classical computers, along with qHEOM simulations. Section 6 concludes the paper with a summary of findings and future directions. Overall, our work demonstrates the potential of a novel quantum computing algorithm to simulate complex non-Markovian dynamics, providing insights into quantum phenomena in chemical systems beyond the limitations of approximate methods.

## 2 Quantum Algorithm for Open Quantum Systems

### 2.1 Time Evolution of the Register State Vector

The state vector  $|\Phi\rangle$  represents the state of the qubits that make up the register of the quantum circuit. Its time evolution is mapped to the evolution of the reduced density matrix elements that describe the non-Markovian dissipative dynamics of the system of interest. To reduce the depth of the circuits, we employ projection operators that allow us to propagate subsets of the reduced density matrix elements. This approach is exact and reduces both the number of gates and the number of qubits required for simulation, allowing for parallel quantum computing of subsets of matrix elements without introducing any approximation.

The procedures for projecting the initialized density matrix elements and encoding them into the state vector  $|\Phi(0)\rangle$  are described in section 3.3. The time-evolved state vector  $|\Phi(t)\rangle$  is obtained as

$$|\Phi(t)\rangle = G(t)|\Phi(0)\rangle, \quad (1)$$

where  $G(t)$  represents the non-unitary propagator corresponding to the numerical method of choice. This non-unitary evolution reflects the open nature of the system interacting with its surrounding environment. As described in section 2.2,  $G(t)$  is implemented as a linear combination of unitaries.

The overall accuracy of the simulation depends on the accuracy of the propagator of choice. Here, we encode the propagator of HEOM which yields numerically exact dynamics, incorporating non-Markovian effects and enabling precise simulations only limited by the number of shots and the level of noise in the quantum device.

### 2.2 Turning the Propagator into Linear Combination of Unitaries

We decompose the non-unitary propagator into a linear combination of unitaries implementing the singular value decomposition (SVD) method proposed by Shlimgen *et al.*<sup>61</sup> The

procedure starts with the SVD of the propagator  $G(t)$ :

$$G(t) = U\Sigma V^\dagger, \quad (2)$$

where  $U$  and  $V$  are unitary matrices and  $\Sigma$  is a diagonal matrix containing the singular values. The singular value matrix  $\Sigma$  is expressed as a linear combination of two diagonal unitary matrices  $\Sigma_+$  and  $\Sigma_-$ ,

$$\Sigma = \frac{\sigma_0}{2}(\Sigma_+ + \Sigma_-), \quad (3)$$

where the diagonal elements of  $\Sigma_+$  and  $\Sigma_-$  are defined as

$$(\Sigma_\pm)_{jj} = \tilde{\sigma}_j \pm i\sqrt{1 - \tilde{\sigma}_j^2}, \quad (4)$$

with  $\tilde{\sigma}_j = \sigma_j/\sigma_0$ . Here,  $\sigma_j$  is the  $j$ -th singular value of  $G(t)$  and  $\sigma_0$  is the largest singular value. Using  $\Sigma_+$  and  $\Sigma_-$ , the propagator  $G(t)$  is decomposed into the linear combination of two unitaries, as follows:

$$G(t) = \frac{\sigma_0}{2}(U\Sigma_+V^\dagger + U\Sigma_-V^\dagger). \quad (5)$$

### 2.3 Quantum Circuit for Non-Unitary Propagation

The linear combination of two unitaries, introduced by eq 5, can be readily implemented by a quantum circuit with a one-qubit dilation, using unitary gates as shown in Fig. 1. To

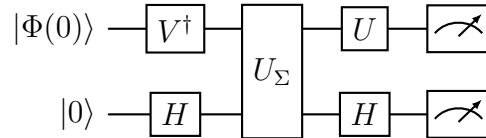


Figure 1: Quantum circuit for SVD dilation, with  $H$  the single qubit Hadamard gate, while  $V$  and  $U$  are defined according to eq 2.

achieve this, we define a diagonal unitary operator  $U_\Sigma = \Sigma_+ \oplus \Sigma_-$  that acts on both the main and ancilla qubits, as follows:

$$U_\Sigma = \begin{pmatrix} \Sigma_+ & 0 \\ 0 & \Sigma_- \end{pmatrix}. \quad (6)$$

The output of the quantum circuit is the following state:

$$\frac{1}{2} \begin{pmatrix} U(\Sigma_+ + \Sigma_-)V^\dagger|\Phi(0)\rangle \\ U(\Sigma_+ - \Sigma_-)V^\dagger|\Phi(0)\rangle \end{pmatrix} = \frac{1}{\sigma_0} \begin{pmatrix} G(t)|\Phi(0)\rangle \\ |\phi\rangle \end{pmatrix}. \quad (7)$$

Therefore, when the ancilla is in state  $|0\rangle$ , we obtain the desired state  $G(t)|\Phi(0)\rangle/\sigma_0 = U(\Sigma_+ + \Sigma_-)V^\dagger|\Phi(0)\rangle/2$  (up to the normalization factor  $\sigma_0$ ). When the ancilla is in state  $|1\rangle$ , we obtain the state  $|\phi\rangle = U(\Sigma_+ - \Sigma_-)V^\dagger|\Phi(0)\rangle/2$ , which is discarded.

## 2.4 Efficient Implementation of Diagonal Unitary Operators Using Walsh Operators

The diagonal unitary  $U_\Sigma$ , introduced by eq 6, entangles the main and ancilla qubits. Upon compilation, this operation typically generates deep circuits which represent the computational bottleneck for computations on NISQ devices. However, efficient implementations of diagonal unitaries can be achieved using the Walsh operator representation.<sup>77</sup> For example, Seneviratne *et al.* have implemented Walsh operators to compile the singular value diagonal matrix of Kraus operators.<sup>35</sup> Here, we apply this technique to optimize the implementation of  $U_\Sigma$ .

$N$ -dimensional ( $N = 2^n$ ) diagonal unitary matrices  $U_\Sigma$ , can be expressed, as follows:

$$U_\Sigma = e^{i\hat{F}}, \quad (8)$$

where  $\hat{F}$  is a real diagonal matrix. Its diagonal elements  $f_k$  define the diagonal elements of  $U_\Sigma$ :  $(U_\Sigma)_{kk} = e^{if_k}$ . When  $U_\Sigma$  is defined according to eq 6, with matrix elements defined according to eq 4, we have  $f_k = \arccos \tilde{\sigma}_k$ , for  $k = 0, 1, \dots, N/2 - 1$ , and  $f_k = -\arccos \tilde{\sigma}_{k-N/2}$ , for  $k = N/2, \dots, N - 1$ .

The real diagonal matrix  $\hat{F}$  can be represented in the  $n$ -qubit Pauli-Z and identity basis through

$$\hat{F} = \sum_{j=0}^{N-1} a_j \hat{w}_j, \quad (9)$$

where  $a_j$ , are the Walsh coefficients, and  $\hat{w}_j$ , are the Walsh operators (*i.e.*, tensor products of the one-qubit identity and Pauli-Z matrices):

$$\hat{w}_j = (\hat{Z}_1)^{j_1} \otimes (\hat{Z}_2)^{j_2} \otimes \dots \otimes (\hat{Z}_n)^{j_n}, \quad (10)$$

where  $(\hat{Z}_l)^0 \equiv \hat{I}$  (identity gate) and  $(\hat{Z}_l)^1 \equiv \hat{Z}$  (Pauli-Z gate), act on the  $l$ -th qubit. Here, " $\otimes$ " is the Kronecker product, while  $j_l \in \{0, 1\}$  are the bits of the binary expansion of  $j$  ( $j = \sum_{l=1}^n j_l 2^{l-1}$ ). The elements of the diagonal matrix  $\hat{w}_j$  are defined as

$$\begin{aligned} [\hat{w}_j]_{kk} &= \langle k | \hat{w}_j | k \rangle, \\ &= \langle k_1 k_2 \dots k_n | \hat{w}_j | k_1 k_2 \dots k_n \rangle, \\ &= \prod_{l=1}^n \langle k_l | (\hat{Z}_l)^{j_l} | k_l \rangle, \\ &= (-1)^{\sum_l j_l k_l}, \end{aligned} \quad (11)$$

where  $k_l \in \{0, 1\}$  are the bits in the binary expansion of  $k$ , with  $k = \sum_{l=1}^n k_l 2^{(n-l)}$ , while  $|k_1 k_2 \dots k_n\rangle = |k_1\rangle \otimes |k_2\rangle \otimes \dots \otimes |k_n\rangle$  with  $|0\rangle = [1, 0]^T$  and  $|1\rangle = [0, 1]^T$ .

The Walsh coefficients  $a_j$  are obtained from the Hilbert-Schmidt inner products of  $\hat{F}$  and



the Walsh operators  $\hat{w}_j$ , as follows:

$$\begin{aligned}
a_j &= \frac{1}{N} \text{Tr} \left[ \hat{w}_j \hat{F} \right], \\
&= \frac{1}{N} \sum_{k=0}^{N-1} [\hat{w}_j]_{kk} f_k, \\
&= \frac{1}{N} \sum_{k=0}^{N-1} (-1)^{\sum_l j_l k_l} f_k.
\end{aligned} \tag{12}$$

This transformation between  $a_j$  and  $f_k$ , introduced by eq 12, is the so-called Walsh–Fourier transform.<sup>78,79</sup>

Having the Walsh representation of  $\hat{F}$ , introduced by eq 9, and noting that Walsh operators commute (*i.e.*,  $[\hat{w}_j, \hat{w}_k] = 0$ ), the  $U_\Sigma$  can be written as

$$U_\Sigma = \prod_{j=0}^{N-1} e^{ia_j \hat{w}_j}. \tag{13}$$

Each gate  $e^{ia_j \hat{w}_j}$  can be readily implemented by using CNOT and Z-rotation gates, as described in Ref. 77. The circuit can be further optimized by recognizing that the gates  $e^{ia_j \hat{w}_j}$  commute. By rearranging the indices  $j$  using the Gray code and leveraging commutation properties of CNOT gates, we can reduce the number of CNOT gates, as implemented in Ref. 77.

## 3 Methods for Open Quantum System Dynamics

### 3.1 Model Hamiltonian

We simulate the dynamics of quantum systems coupled to harmonic baths, as described by the Hamiltonian

$$H_T = H_S + H_B + H_I, \tag{14}$$

where  $H_S$  is the Hamiltonian of the system,  $H_B$  is the bath Hamiltonian, and  $H_I$  describes the system-bath interaction. We assume that the bath consists of harmonic modes and that the system-bath coupling is linear in the coordinates of these modes, such that:

$$\begin{aligned}
H_B &= \sum_{mj} \frac{p_{mj}^2}{2M_{mj}} + \frac{1}{2} M_{mj} \omega_{mj}^2 x_{mj}^2, \\
H_I &= \sum_m A_m \otimes B_m \equiv - \sum_m A_m \otimes \sum_j c_{mj} x_{mj}.
\end{aligned}
\tag{15}$$

Here, to maintain generality, we consider multiple distinct harmonic baths indexed by  $m$ . Each bath contains multiple modes, where  $x_{mj}$ ,  $p_{mj}$ ,  $M_{mj}$ , and  $\omega_{mj}$  are the coordinate, momentum, mass, and frequency of the  $j$ -th mode in the  $m$ -th bath. The Hermitian system operator  $A_m$  couples to the collective coordinate  $B_m = - \sum_j c_{mj} x_{mj}$  of the  $m$ -th bath, with the coupling strength between the system and the  $mj$ -th bath mode being given by  $c_{mj}$ .

For the aforementioned system-bath model, the influence of the environment on the system can be fully characterized by the reservoir correlation function:<sup>1,3,80</sup>

$$C(t) = \frac{1}{\pi} \int_0^\infty d\omega J(\omega) [\coth(\frac{\beta\omega}{2}) \cos(\omega t) - i \sin(\omega t)], \tag{16}$$

where  $\beta = (k_B T)^{-1}$  is the inverse temperature, and  $J(\omega)$  is the spectral density, defined as

$$J(\omega) = \frac{\pi}{2} \sum_j \frac{c_j^2}{M_j \omega_j} \delta(\omega - \omega_j) . \tag{17}$$

For simplicity, we consider the environment to be identical for each  $m$  ( $c_{mj} \equiv c_j$ ), thus omitting the dependence on  $m$  for  $C(t)$  and  $J(\omega)$ . Finally, we assume the spectral density has a Debye form:

$$J(\omega) = \frac{\eta \omega \omega_c}{\omega^2 + \omega_c^2}, \tag{18}$$

where  $\eta$  is the coupling strength, and  $\omega_c$  characterizes the width of the spectral density.

### 3.2 Hierarchical Equations of Motion

The HEOM approach decomposes the reservoir correlation function into a sum of exponentials:

$$C(t) = \sum_k d_k e^{-v_k t} , \quad (19)$$

where  $v_k$  and  $d_k$  are the frequencies and coefficients of the effective modes, respectively. For the Debye spectral density,  $v_k$  and  $d_k$  are analytically given by:<sup>22,81</sup>

$$v_1 = \omega_c , \quad (20)$$

$$v_k \equiv \frac{2\pi(k-1)}{\beta} ; \quad k > 1, \quad (21)$$

and

$$d_1 = \frac{\eta\omega_c}{2} [\cot(\beta\omega_c/2) - i] , \quad (22)$$

$$d_k = \frac{2}{\beta} \frac{\eta v_k \omega_c}{v_k^2 - \omega_c^2} ; \quad k > 1. \quad (23)$$

This decomposition transforms the original model of a system coupled to infinite bath modes into a model of a system interacting with a finite number of effective modes.<sup>59,82,83</sup>

In HEOM, the density matrices can be combined into a single state vector in the tensor product Hilbert space of the system and effective modes, as follows:

$$|\Psi\rangle = \sum_{\mathbf{n}, p, q} \rho_{\mathbf{n}}(p, q) |p\rangle |\tilde{q}\rangle |\mathbf{n}\rangle , \quad (24)$$

where  $|\mathbf{n}\rangle$  defines the state of the effective modes, with  $\mathbf{n} = \{n_1, n_2, \dots, n_{mk}, \dots\}$ . The states  $|p\rangle \in \mathcal{H}_S$  and  $|\tilde{q}\rangle \in \tilde{\mathcal{H}}_S$  belong to the Hilbert space of the system, and its corresponding fictitious twin space, respectively, as formulated by thermo-field theory.<sup>84</sup> This representation of a density matrix as a state vector is also known as purification in quantum computing.<sup>48,85,86</sup>

The coefficients  $\rho_{\mathbf{n}}(p, q) = \langle p | \hat{\rho}_{\mathbf{n}} | q \rangle$ , introduced by eq 24, are the matrix elements of

the density operator in the system Liouville space. The coefficient  $\rho_{\mathbf{0}}(p, q)$ , with  $\mathbf{n} \equiv \{0, 0, \dots, 0\}$ , corresponds to the reduced density operator (RDO), defined as the partial trace of the total density operator  $\rho_T(t)$  over the bath degrees of freedom:  $\rho(t) = \text{Tr}_B[\rho_T(t)]$ . This RDO describes the evolution of the reduced system.

With the twin-space formulation of thermo-field theory, the HEOM can be written as a time-dependent Schrödinger-like equation for the evolution of  $|\Psi\rangle$ ,<sup>82,87</sup>

$$\frac{d|\Psi\rangle}{dt} = -i\mathbb{H}|\Psi\rangle, \quad (25)$$

where the effective Hamiltonian  $\mathbb{H}$  is

$$\begin{aligned} \mathbb{H} = & \hat{H}_S - \tilde{H}_S - i \sum_{mk} v_k \hat{b}_{mk}^\dagger \hat{b}_{mk} + \sum_{mk} \hat{A}_m \left( \sqrt{r_k} \hat{b}_{mk} + \frac{d_k}{\sqrt{r_k}} \hat{b}_{mk}^\dagger \right) \\ & - \sum_{mk} \tilde{A}_m \left( \sqrt{r_k} \hat{b}_{mk} + \frac{d_k^*}{\sqrt{r_k}} \hat{b}_{mk}^\dagger \right). \end{aligned} \quad (26)$$

Operators with hats ( $\hat{O}$ ) act on the system Hilbert space, while tilded operators ( $\tilde{O}$ ) act on the fictitious space:  $\hat{O}|i\rangle|\tilde{j}\rangle \equiv O \otimes I|i\rangle|\tilde{j}\rangle$ , and  $\tilde{O}|i\rangle|\tilde{j}\rangle \equiv I \otimes O^T|i\rangle|\tilde{j}\rangle$ , where  $I$  is the identity operator. Creation and annihilation operators for the effective modes satisfy

$$\begin{aligned} \hat{b}_{mk}^\dagger |n_1, \dots, n_{mk}, \dots\rangle &= \sqrt{n_{mk} + 1} |n_1, \dots, n_{mk} + 1, \dots\rangle, \\ \hat{b}_{mk} |n_1, \dots, n_{mk}, \dots\rangle &= \sqrt{n_{mk}} |n_1, \dots, n_{mk} - 1, \dots\rangle. \end{aligned} \quad (27)$$

The scaling factor  $r_k$  allows flexible definitions of the operators (if  $[\hat{b}_{mk}, \hat{b}_{mk}^\dagger] = 1$  then  $[\sqrt{r_k} \hat{b}_{mk}, \frac{\hat{b}_{mk}^\dagger}{\sqrt{r_k}}] = 1$  still satisfies the commutation relation). For this work, we use  $r_k = |d_k|$ , corresponding to the efficient filtering algorithm by Shi *et al.*<sup>22,88</sup>

In practice, the number of effective modes  $K$  (*i.e.*, the number of terms in the decomposition in eq 19) and the Fock space size  $L$  defining the truncation of the basis for each effective mode, with  $n_{mk} \leq L$ , need to be limited. We ensure convergence by increasing both parameters until stable results are achieved. For our model systems in this work,

$K \leq 5$  is sufficient. However, for more complex spectral densities or lower temperatures, larger values of  $K$  might be required, posing computational challenges. Those challenges could be addressed by recent advances, such as Tensor-Train methods,<sup>23,82,89,90</sup> and more advanced reservoir correlation function decomposition schemes (e.g., Padé spectrum decomposition,<sup>91,92</sup> Fano spectrum decomposition (FSD),<sup>93,94</sup> barycentric spectrum decomposition (BSD),<sup>14,95</sup> Prony fitting decomposition (PFD),<sup>96</sup> and others.<sup>97–100,100–104</sup>).

### 3.3 The Projected Propagator

In this section, we present the general method for calculating the propagator  $G(t)$ , introduced by eq 1, using the HEOM method.

As described in section 3.2, the HEOM method casts the effect of the bath on the system in terms of a small number of effective modes, thereby significantly reducing the computational cost. However, the Hilbert space of the state vector  $|\Psi\rangle$  can still be very large. Therefore, we further reduce the dimensionality of the problem by projecting  $|\Psi\rangle$  onto a smaller subspace, as described in Section 2.1. The projected state vector is then encoded into the state vector of qubits,

$$|\Phi\rangle = \mathcal{M}(\mathcal{P}|\Psi\rangle), \quad (28)$$

where  $\mathcal{P}$  is the projection operator that projects the state  $|\Psi\rangle$  onto a subspace corresponding to the relevant physical quantities.  $\mathcal{M}$  maps the projected subspace state  $\mathcal{P}|\Psi\rangle$  to the qubit state vector  $|\Phi\rangle$ .

We use the following projection operator:

$$\mathcal{P} = \sum_{pq \in S} |p\tilde{q}\rangle |\mathbf{0}\rangle \langle p\tilde{q}| \langle \mathbf{0}|, \quad (29)$$

where  $S$  is the subspace containing all the states relevant to the physical quantities of interest.

The mapping  $\mathcal{M}$  then encodes states in this subspace into qubit states, as follows:

$$\mathcal{M} : |p_j \tilde{q}_j\rangle |0\rangle \rightarrow |j_n, \dots, j_1\rangle, \quad (30)$$

where  $p_j q_j$  is the  $j$ -th element in  $S$ , and  $(j_n, \dots, j_1)$  represents the  $n$ -bit binary form of the integer  $j$ . Here,  $n = \log_2 N_S$  gives the number of qubits required to encode the  $N_S$  relevant states in  $S$ . Consequently, the state  $|p_j \tilde{q}_j\rangle |0\rangle$  is encoded as the qubit state  $|j_n, \dots, j_1\rangle$ . A schematic representation of the projection and encoding processes is shown in Figure 2.

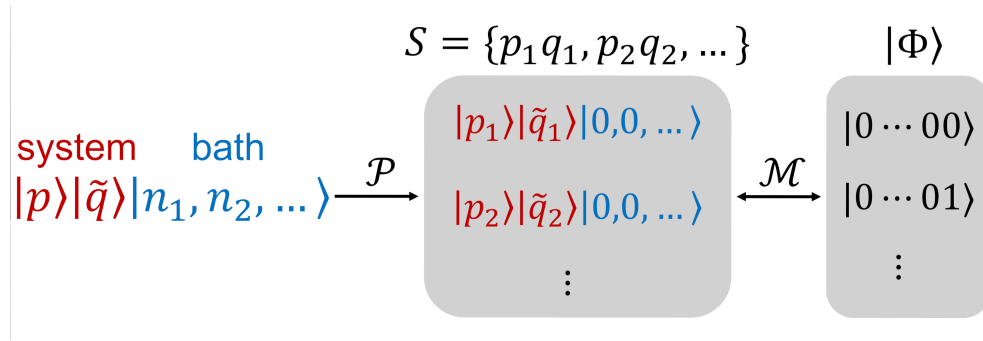


Figure 2: Illustration of the projection and encoding processes. The HEOM computational space is projected by  $\mathcal{P}$  onto a subspace where all effective modes are in state  $|0\rangle$ . The subspace is defined by the set  $S$ , which includes states relevant to the physical quantities of interest. The states within this subspace are further encoded into the qubit state vector  $|\Phi\rangle$ , with each qubit in either  $|0\rangle$  or  $|1\rangle$ .

The propagator in the reduced space has dimensions  $N_S \times N_S$  and is given by:

$$G(t) = \mathcal{M} \mathcal{P} e^{-i\mathbb{H}t} \mathcal{P} \mathcal{M}^\dagger, \quad (31)$$

where  $\mathbb{H}$  is the effective Hamiltonian of HEOM defined in eq 26.

It should be noted that the dynamics within the subspace  $S$  is still numerical exact, in the sense that the numerical exact HEOM (*i.e.*,  $e^{-i\mathbb{H}t}$  in eq 31) governs the evolution of the subspace elements. Simulations of physical quantities of interest require a suitable choice of projection operators to the corresponding subspace of those physical properties.

### 3.4 The Lindblad Quantum Master Equation

The Lindblad equation is widely used in the field of quantum information science to model decoherence and open quantum system dynamics.<sup>56–58,61,65,68,70–73</sup> However, the validity of the Lindblad equation, which rests on several rather restrictive assumptions, is rarely tested. In what follows, we perform such a test by comparing and contrasting the predictions of the Lindblad equation to those of the numerically exact HEOM for the model systems under consideration.

For an open quantum system governed by the Hamiltonian given in eqs 14 and 15, the Lindblad equation can be derived in the limit of weak system-bath coupling, Markovian dynamics, and subject to the rotating wave approximation (RWA), and takes the following form:<sup>1,8,105</sup>

$$\frac{d\rho(t)}{dt} = -i[H_S + H_{LS}, \rho(t)] + \sum_{\omega} \sum_m \gamma_m(\omega) \left( A_m(\omega)\rho(t)A_m^\dagger(\omega) - \frac{1}{2}\{A_m^\dagger(\omega)A_m(\omega), \rho(t)\} \right). \quad (32)$$

Here,  $\rho(t)$  is the reduced density operator that describes the state of the system and  $[\cdot, \cdot]$  and  $\{\cdot, \cdot\}$  correspond to the commutator and anti-commutator, respectively.  $H_{LS}$  is the Lamb shift Hamiltonian given by eq 35,<sup>1</sup> which accounts for the energy shift induced by the interaction with the environment, and commutes with the system Hamiltonian (*i.e.*,  $[H_S, H_{LS}] = 0$ ).  $\{\gamma_m(\omega)\}$  and  $\{A_m(\omega)\}$  are damping rate coefficients and system jump operators, respectively, which are given by:

$$\gamma_m(\omega) = \int_{-\infty}^{\infty} dt e^{i\omega t} C_m(t), \quad (33)$$

$$A_m(\omega) = \sum_{\epsilon' - \epsilon = \omega} \langle \epsilon | A_m | \epsilon' \rangle | \epsilon \rangle \langle \epsilon' |, \quad (34)$$

$$H_{LS} = \sum_{\omega} \sum_m S_m(\omega) A_m^\dagger(\omega) A_m(\omega), \quad (35)$$

Here,  $\omega = \epsilon' - \epsilon$ , where  $\epsilon$  and  $\epsilon'$  are the eigenvalues of  $H_S$ , corresponding to the eigenstates

$|\epsilon\rangle$  and  $|\epsilon'\rangle$ , respectively, and  $C_m(t)$  is the bath correlation function defined in eq 16. Here we explicitly reintroduce the subscript  $m$  to indicate that it corresponds to the correlation function of the  $m$ -th bath, which is coupled to the system through the operator  $A_m$ . Finally,  $S_m(\omega)$  is given by:

$$S_m(\omega) = \frac{1}{2i}(\Gamma_m(\omega) - \Gamma_m^*(\omega)) , \quad (36)$$

$$\Gamma_m(\omega) = \int_0^\infty dt e^{i\omega t} C_m(t) . \quad (37)$$

Importantly, the validity of the Lindblad equation relies on three critical approximations.<sup>8,106</sup> First, the Born approximation assumes weak system-bath coupling within the framework of second-order perturbation theory. Second, the Markovian approximation assumes that the timescale of bath fluctuations is much faster than the timescale of the system's damping. Third, the RWA assumes that rapidly oscillating terms, compared to the time scale of the system's dynamics can be neglected.

The popularity of the Lindblad equation can be traced back to the fact that the description of open quantum system dynamics becomes analytically tractable under those approximations. However, the restrictive nature of those assumptions requires validation, particularly when applied to ultrafast processes of molecular systems such as electronic charge and energy transfer where those assumptions might break down (see below).

## 4 Model Systems for Charge and Energy Transfer

In what follows, we will demonstrate the accuracy and utility of the quantum algorithm described in section 2 by applying it to models of charge transfer in a solvated molecular triad and excitation energy transfer in the FMO complex. Figure 3 provides schematic representations of the model systems. For those model systems, the system corresponds to the electronic degrees of freedom, while the nuclear degrees of freedom play the role of the bath. Furthermore, the system-bath coupling plays a crucial role in determining the rates



of charge and energy transfer in both cases. Below, we outline the Hamiltonians for the two model systems under consideration.

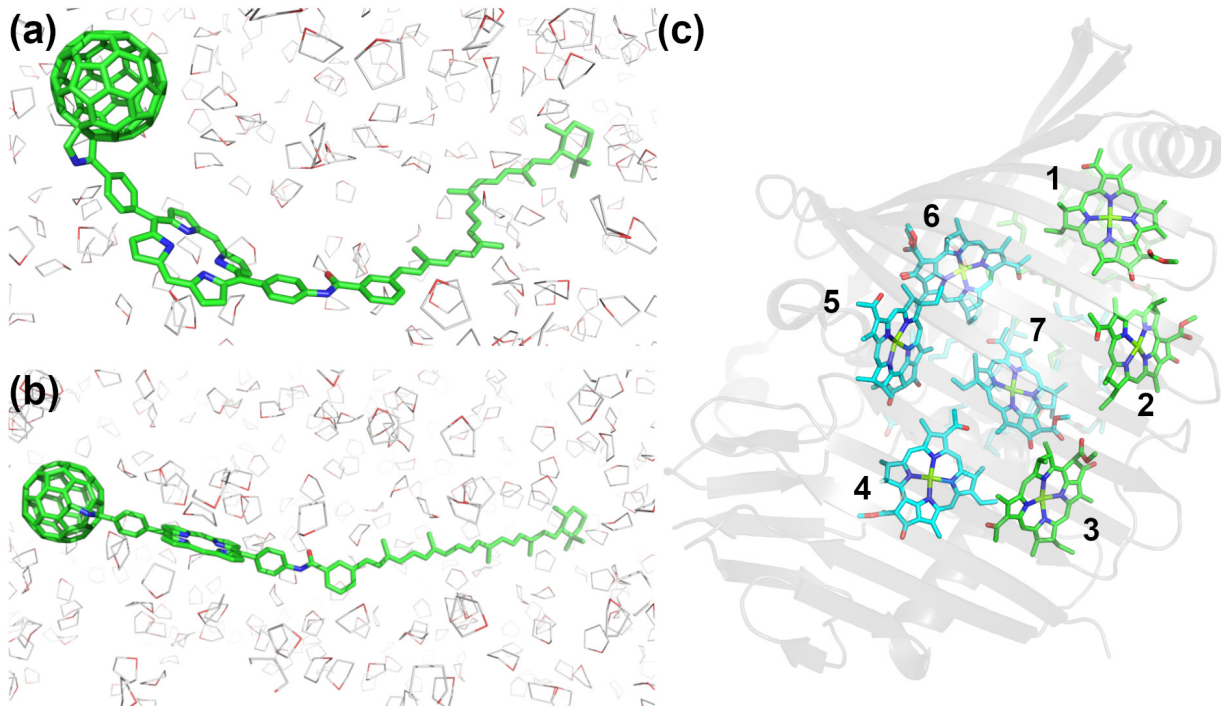


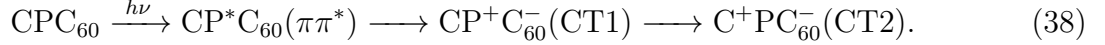
Figure 3: Schematic representation of model systems for electron and energy transfer. (a) Bent conformation and (b) linear conformation of the carotenoid-porphyrin- $C_{60}$  ( $CPC_{60}$ ) molecular triad dissolved in tetrahydrofuran. Charge transfer can occur after photoexcitation of the molecular triad. (c) The FMO complex, where two pathways exist for excitation energy transfer: starts at site 1, transferring through site 2 to site 3, or starts at site 6 and passes through sites 5, 7, and 4, then reaching site 3.<sup>107</sup>

#### 4.1 Model Hamiltonian for Charge Transfer in a Molecular Triad

The first model we examine is photoinduced charge transfer within the carotenoid-porphyrin- $C_{60}$  ( $CPC_{60}$ ) molecular triad dissolved in tetrahydrofuran, which has been recently investigated extensively using a variety of semiclassical rate theories based on inputs from molecular dynamics simulations and time-dependent density functional theory (TDDFT) calculations.<sup>74,108–114</sup>

Upon photoexcitation, the  $CPC_{60}$  transitions from its ground state to the porphyrin-

localized excited  $\pi\pi^*$  state,  $\text{CP}^*\text{C}_{60}$ . The system subsequently undergoes electron transfer from the porphyrin to the  $\text{C}_{60}$ , to form the so-called CT1 state,  $\text{CP}^+\text{C}_{60}^-$ . Further hole transfer from the porphyrin to the carotene subsequently leads to the formation of the so-called CT2 state,  $\text{C}^+\text{PC}_{60}^-$  state.<sup>108</sup> This sequence of events from photoexcitation to the formation of CT2 can then be summarized as follows:



Two dominant characteristic conformations were reported when  $\text{CPC}_{60}$  is dissolved in liquid tetrahydrofuran.<sup>108</sup> These conformations are denoted *bent* and *linear* and are shown in Figure 3(a) and (b), respectively. Importantly, the charge transfer rates are conformation-dependent.

In what follows, we will focus on the rate of the  $\pi\pi^* \rightarrow \text{CT1}$  charge transfer process. To this end, we map the system onto a spin-boson model with a Hamiltonian of the following form:<sup>74</sup>

$$H_T = V\sigma_x + E_0\sigma_z + \sum_j \frac{p_j^2}{2M_j} + \frac{1}{2}M_j\omega_j^2(x_j - \frac{c_j}{\omega_j^2}\sigma_z)^2. \quad (39)$$

Here, the donor state  $\pi\pi^*$  is represented as  $|D\rangle = [1, 0]^T$ , and the acceptor state CT1 as  $|A\rangle = [0, 1]^T$ . The electronic coupling between these states is denoted by  $V$ , while  $E_0$  represents the energy difference between these two electronic states. Therefore, considering eqs 14 and 15, the subsystem Hamiltonian is  $H_S = V\sigma_x + E_0\sigma_z$ , with no dependence on  $m$ ,  $A_m = \sigma_z$ . The intramolecular and intermolecular (solvent) nuclear degrees of freedom are treated as a harmonic bath linearly coupled to the system. The initial state is chosen to be

$$\rho_T(t=0) = |D\rangle\langle D| \otimes \frac{e^{-\beta H_B}}{\text{Tr}_B[e^{-\beta H_B}]}, \quad (40)$$

where  $\rho_T(t=0)$  is the total density operator, and the bath DOFs are at thermal equilibrium. The coupling strength ( $\eta$ ) and the width  $\omega_c$  of the spectral density in eq 18 are chosen to

match the reorganization energy and the width of the spectral density from Ref. 74. Table 1 lists the parameters for the  $\pi\pi^* \rightarrow$  CT1 charge transfer process corresponding to the bent and linear conformations of the molecular triad in tetrahydrofuran.

Table 1: The model parameters of the spin-boson model correspond to the  $\pi\pi^* \rightarrow$  CT1 charge transfer process for the bent and linear conformations of the CPC<sub>60</sub> in tetrahydrofuran solution.<sup>74</sup>

Parameter	Bent	Linear
$V$	$2.4 \times 10^{-2}$ eV	$9.0 \times 10^{-3}$ eV
$E_0$	0.507 eV	0.236 eV
$\eta$	0.2565 eV	0.318 eV
$\omega_c$	25 cm <sup>-1</sup>	25 cm <sup>-1</sup>
T	300 K	300 K

The charge transfer dynamics in CPC<sub>60</sub> were simulated via the numerically exact HEOM framework, eq 25, as well as via the approximate Lindblad equation, eq 32. In the HEOM simulations, the initial state was set according to eq 40, with  $|\Psi_{MT}(t = 0)\rangle = |D\rangle|\tilde{D}\rangle|\mathbf{0}\rangle$ . The effective Hamiltonian for HEOM is

$$\mathbb{H}_{MT} = \hat{H}_S - \tilde{H}_S - i \sum_{k=1}^K v_k \hat{b}_k^\dagger \hat{b}_k + \hat{\sigma}_z \sum_{k=1}^K \left( \sqrt{r_k} \hat{b}_k + \frac{d_k}{\sqrt{r_k}} \hat{b}_k^\dagger \right) - \tilde{\sigma}_z \sum_{k=1}^K \left( \sqrt{r_k} \hat{b}_k + \frac{d_k^*}{\sqrt{r_k}} \hat{b}_k^\dagger \right), \quad (41)$$

where ‘‘MT’’ denotes the molecular triad model.

## 4.2 Model Hamiltonian for Energy Transfer in the FMO Complex

The Fenna-Matthews-Olson (FMO) complex is a well-characterized light-harvesting system<sup>80,107,115–119</sup> that serves as a quantum conduit, directing excitation energy from the light-harvesting antenna to the reaction center.<sup>120,121</sup> This process involves exciton transfer

between the seven bacteriochlorophyll (Bchl) chromophores comprising the FMO complex. Figure 3(c) provides a schematic representation of the system.

FMO is often described in terms of a Frenkel exciton Hamiltonian:

$$\begin{aligned}
H_{FMO} = & \sum_{m=1}^N \epsilon_m |m\rangle\langle m| + \sum_{m<n} J_{mn} (|m\rangle\langle n| + |n\rangle\langle m|) \\
& + \sum_{m=1}^N \sum_{j=1}^{N_b^m} \left( \frac{p_{mj}^2}{2M_{mj}} + \frac{1}{2} M_{mj} \omega_{mj}^2 x_{mj}^2 - c_{mj} x_{mj} |m\rangle\langle m| \right). \tag{42}
\end{aligned}$$

Here,  $|m\rangle$  represents the excited state of site  $m$ , which corresponds to locally exciting the  $m$ -th BChl chromophore.  $\epsilon_m$  is the site excitation energy, and  $J_{mn}$  denotes the dipolar coupling between sites  $m$  and  $n$ . Each site is coupled to its phonon bath, with  $N_b^m$  phonon modes per bath. The parameter  $c_{mj}$  defines the coupling strength of phonon mode  $j$  to site  $m$ . Following eqs. 14 and 15, we identify  $H_S = \sum_{m=1}^N \epsilon_m |m\rangle\langle m| + \sum_{m<n} J_{mn} (|m\rangle\langle n| + |n\rangle\langle m|)$  as the system Hamiltonian, and  $A_m = |m\rangle\langle m|$ .

In this study, we use the seven-site model Hamiltonian ( $N = 7$ ) for the FMO complex, with  $\epsilon_m$  and  $J_{mn}$  values obtained from Moix. *et al.*<sup>117</sup> The matrix representation of  $H_S$  (in units of  $\text{cm}^{-1}$ ) is

$$H_S = \begin{pmatrix} 310.0 & -97.9 & 5.5 & -5.8 & 6.7 & -12.1 & -10.3 \\ -97.9 & 230.0 & 30.1 & 7.3 & 2.0 & 11.5 & 4.8 \\ 5.5 & 30.1 & 0 & -58.8 & -1.5 & -9.6 & 4.7 \\ -5.8 & 7.3 & -58.8 & 180.0 & -64.9 & -17.4 & -64.4 \\ 6.7 & 2.0 & -1.5 & -64.9 & 405.0 & 89.0 & -6.4 \\ -12.1 & 11.5 & -9.6 & -17.4 & 89.0 & 320.0 & 31.7 \\ -10.3 & 4.8 & 4.7 & -64.4 & -6.4 & 31.7 & 270.0 \end{pmatrix}. \tag{43}$$

For the bath, each site couples to an identical bath (*i.e.*,  $c_{mj} \equiv c_j$ ) and follows a Debye spectral density with parameters  $\eta = 70 \text{ cm}^{-1}$  and  $\omega_c^{-1} = 50 \text{ fs}$ .<sup>23,107,122</sup>

Excitation energy transfer within the FMO complex follows two primary pathways: either starting at site 1 and passing through site 2 to site 3, or starting at site 6 and passing through sites 5, 7, and 4, to reach site 3.<sup>107</sup> We focus on the first pathway, where the initial state is  $|m = 1\rangle$  and the phonon bath is at thermal equilibrium:

$$\rho_T(t = 0) = |1\rangle\langle 1| \otimes \frac{e^{-\beta H_B}}{\text{Tr}_B[e^{-\beta H_B}]} . \quad (44)$$

In this setup, the initial HEOM state vector is  $|\Psi_{FMO}(t = 0)\rangle = |1\rangle|\tilde{1}\rangle|\mathbf{0}\rangle$ , and effective Hamiltonian is expressed as

$$\begin{aligned} \mathbb{H}_{FMO} = & \hat{H}_S - \tilde{H}_S - i \sum_{m=1}^N \sum_{k=1}^K v_k \hat{b}_{mk}^\dagger \hat{b}_{mk} + \sum_{m=1}^N \sum_{k=1}^K |m\rangle\langle m| \left( \sqrt{r_k} \hat{b}_{mk} + \frac{d_k}{\sqrt{r_k}} \hat{b}_{mk}^\dagger \right) \\ & - \sum_{m=1}^N \sum_{k=1}^K |\tilde{m}\rangle\langle \tilde{m}| \left( \sqrt{r_k} \hat{b}_{mk} + \frac{d_k^*}{\sqrt{r_k}} \hat{b}_{mk}^\dagger \right) , \end{aligned} \quad (45)$$

where ‘‘FMO’’ stands for the FMO complex.

## 5 Results

To assess the applicability of the Lindblad equation, we first tested a general spin-boson model (eq 39) with tunable parameters. Figure 4 compares the dynamics of the donor state population at different system-bath coupling strengths  $\eta$ , as obtained via the Lindblad quantum master equation vs. the numerically exact HEOM method (the values of the remaining model parameters are set at  $V = 0.5$ ,  $E_0 = 2.5$ ,  $\beta = 1$ , and  $\omega_c = 1$ ). The inset provides a detailed view of the short-time dynamics. As expected, the Lindblad quantum master equation is seen to be accurate when  $\eta$  is sufficiently small (the weak system-bath coupling limit). Increasing the value of  $\eta$  beyond the weak coupling limit ( $\eta \sim 0.01 - 0.05$ ), the Lindblad quantum master equation is found to overestimate the population relaxation rate at short times and underestimate it at longer times.

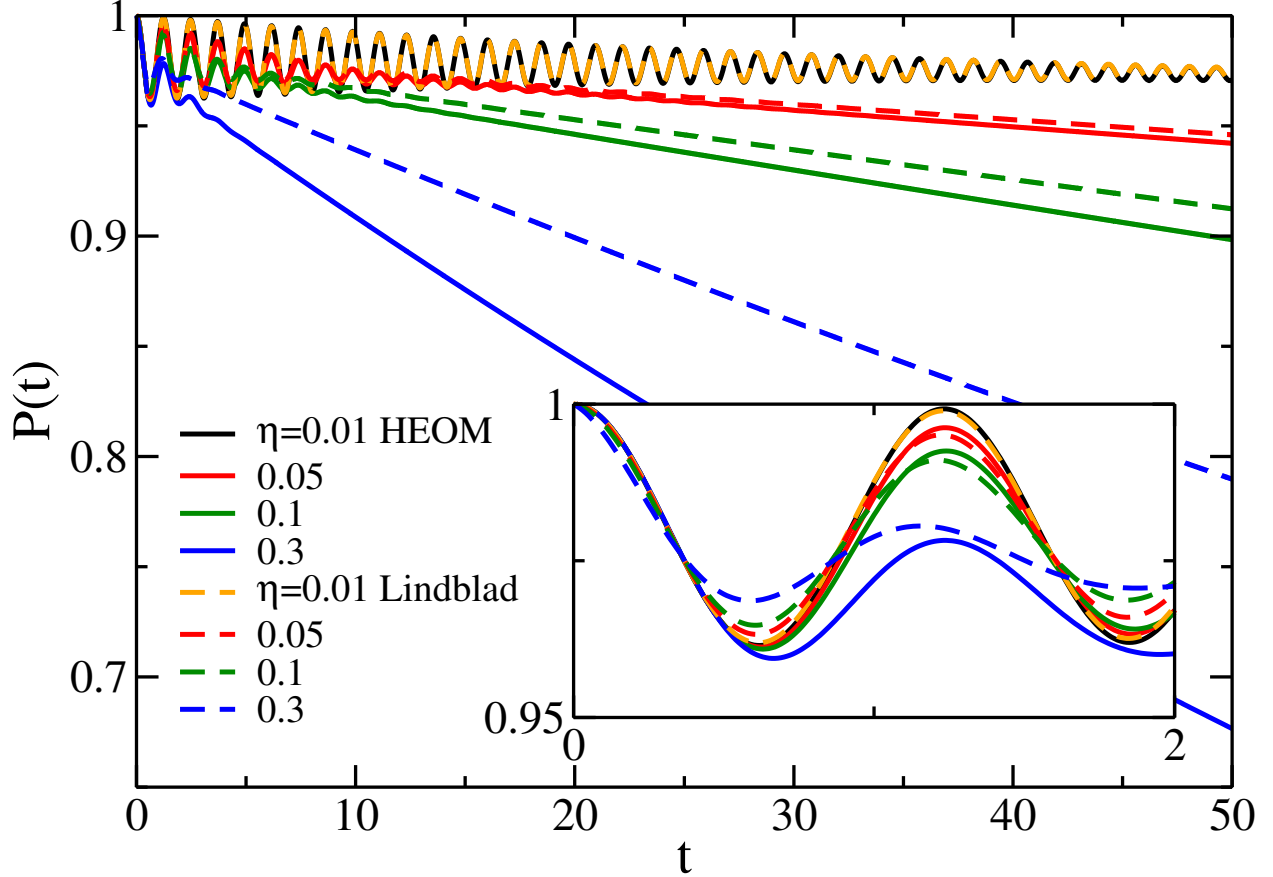


Figure 4: Population dynamics  $P(t)$  of the donor state in the spin-boson model across various system-bath coupling strengths  $\eta$ , computed using numerically exact HEOM (solid lines) and the Lindblad equation (dashed lines). Simulation parameters:  $V = 0.5$ ,  $E_0 = 2.5$ ,  $\beta = 1$ ,  $\omega_c = 1$ . The inset highlights the transient dynamics in detail.

It should also be noted that the dynamical range of validity of the Lindblad quantum master equation corresponds to a weak damping regime, and therefore gives rise to donor population dynamics that are pronouncedly coherent (oscillatory) and dominated by the electronic coupling  $V$ . While damping increasingly dominates the dynamics with increasing  $\eta$ , the regime where the dynamics are truly incoherent lies outside the range of validity of the Lindblad quantum master equation. The breakdown of the Lindblad equation at strong system-environment coupling  $\eta$  is consistent with the fact that it relies on the Born-Markov approximation.<sup>1</sup> As noted in previous studies, perturbative methods become invalid when the perturbation strength is strong.<sup>13,123–125</sup> The results in Figure 4 clearly demonstrate

that the Lindblad quantum master equation is only applicable within the coherent dynamics regime ( $\eta \ll V$ ).

### 5.1 Charge Transfer in a Molecular Triad: Lindblad vs. HEOM

We now apply the Lindblad equation and HEOM to study electron transfer in the molecular triad. Figure 5 shows the donor state ( $\pi\pi^*$ ) population dynamics for the  $\pi\pi^* \rightarrow \text{CT1}$  charge transfer process of  $\text{CPC}_{60}$  in tetrahydrofuran solution. Simulation parameters for the two  $\text{CPC}_{60}$  conformations (bent and linear) are provided in Table 1.

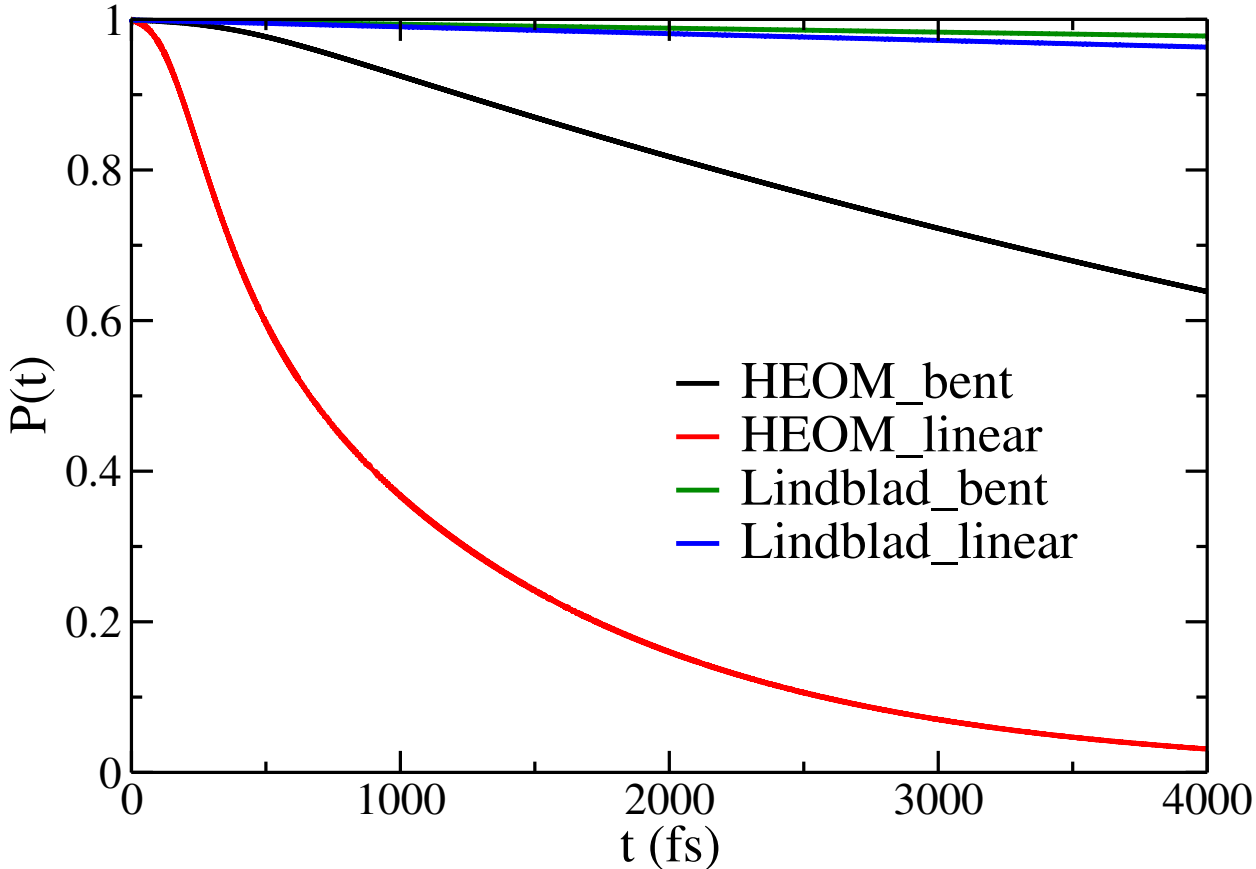


Figure 5:  $\pi\pi^*$  state population dynamics in the  $\pi\pi^* \rightarrow \text{CT1}$  photoinduced charge transfer process of  $\text{CPC}_{60}$  molecular triad dissolved in tetrahydrofuran. Here, the simulation results using the Lindblad equation and the numerically exact HEOM are shown for the two conformations of the  $\text{CPC}_{60}$  molecular triad (bent and linear). The parameters used in the simulations are in Table 1.

Table 2: Charge transfer rate constants calculated by the HEOM, the Lindblad equation, and the Marcus theory. The HEOM and Lindblad rate constants are obtained by exponential fitting of their respective  $P(t)$  data in Figure 5, in the range of  $t = 3000$  to  $4000$  fs.

Rate constant	HEOM	Lindblad	Marcus
Bent	$1.24 \times 10^{11} \text{ s}^{-1}$	$5.32 \times 10^9 \text{ s}^{-1}$	$1.19 \times 10^{11} \text{ s}^{-1}$
Linear	$8.17 \times 10^{11} \text{ s}^{-1}$	$9.20 \times 10^9 \text{ s}^{-1}$	$1.13 \times 10^{12} \text{ s}^{-1}$

Inspection of the exact HEOM results shows that, for both bent and linear conformations, the population dynamics follow incoherent rate kinetic ( $\eta \gg V$ ), with the long-time population of the  $\pi\pi^*$  state exhibiting an exponential decay. Notably, the  $\pi\pi^* \rightarrow \text{CT1}$  electron transfer is significantly faster in the linear conformation, which is consistent with previous studies.<sup>108</sup> In contrast, the Lindblad quantum master equation predicts much slower charge transfer rates for both conformations, which is consistent with the fact that  $\eta \gg V$  for this model (see Table 1). Despite these discrepancies, the Lindblad quantum master equation does capture some trends, such as the exponential decay in population dynamics and the faster charge transfer rate in the linear conformation.

To quantitatively illustrate the discrepancy between the predictions of the Lindblad quantum master equation and the exact results, we present the charge transfer rate constants predicted by HEOM and the Lindblad equation in Table 2. The rate constants are obtained from an exponential fit of the  $P(t)$  data in Figure 5 over the time range  $t = 3000$  to  $4000$  fs. For comparison, we also include rate constants calculated using Marcus theory.<sup>126–128</sup> According to Marcus theory, the charge transfer rate constant  $k_{\text{Marcus}}$  is given by:<sup>2,74,126–128</sup>

$$k_{\text{Marcus}} = \frac{V^2}{\hbar} \sqrt{\frac{\pi}{\lambda kT}} e^{-\frac{(E_{DA}-\lambda)^2}{4\lambda kT}}, \quad (46)$$

where  $E_{DA} = 2E_0$  is the energy difference between the donor and acceptor states, and  $\lambda$  is the reorganization energy. For a spin-boson model with Debye spectral density (eq 18),  $\lambda = 2\eta$ .<sup>22</sup> The Marcus rate constants in Table 2 are consistent with those reported by Tong *et al.*<sup>74</sup> Our  $\pi\pi^*$  state dynamics results for the bent conformation also align with the cavity-free



case in Ref. 18, where minimal population change was observed within 5000 a.u. (120.9 fs); here, significant dynamics emerge only beyond the 1000 fs timescale.

As shown in Table 2, the exact HEOM rate constants closely match the Marcus rate constants, underscoring Marcus theory’s robustness in describing charge transfer in solution and validating the spin-boson model parameters in Table 1 and the HEOM results. In contrast, the Lindblad equation predicts significantly slower transfer rates, one to two orders of magnitude lower than the exact (HEOM) rates. This discrepancy is more pronounced for the linear conformation, with  $k_{HEOM}/k_{Lindblad}$  values of 23.3 for the bent conformation and 88.8 for the linear conformation.

This outcome is expected. From Figure 4, we observed that the Lindblad equation is only accurate when  $\eta \ll V$ , suggesting  $\eta/V$  as a key parameter for assessing its validity. Table 1 shows  $\eta/V = 10.7$  for the bent conformation and  $\eta/V = 35.3$  for the linear conformation. These values indicate that the deviation between the Lindblad and exact rates ( $k_{HEOM}/k_{Lindblad}$ ) is indeed proportional to  $\eta/V$ .

## 5.2 Energy Transfer in the FMO Complex: Lindblad vs. HEOM

In Figure 6, we compare Lindblad dynamics with the numerically exact HEOM dynamics for excitation energy transfer in the FMO complex at 300 K. We present the population dynamics across different sites, with the initial population localized at site 1. Simulation parameters are specified in section 4.2.

The HEOM results in Figure 6 show that within the transient dynamics regime ( $t < 300$  fs), coherent oscillations occur between sites 1 and 2. These oscillations fade over longer timescales, transitioning into a rate kinetics regime at longer times. As the population at site 3 grows, signifying energy transfer toward the terminal site and subsequently to the reaction center.<sup>117</sup> This behavior stems from the fact that  $\eta \sim J_{mn}$  in this case.

The fact that  $\eta \sim J_{mn}$  in FMO is also consistent with the observation that the Lindblad dynamics in Figure 6 are in better agreement with the exact HEOM results (in comparison

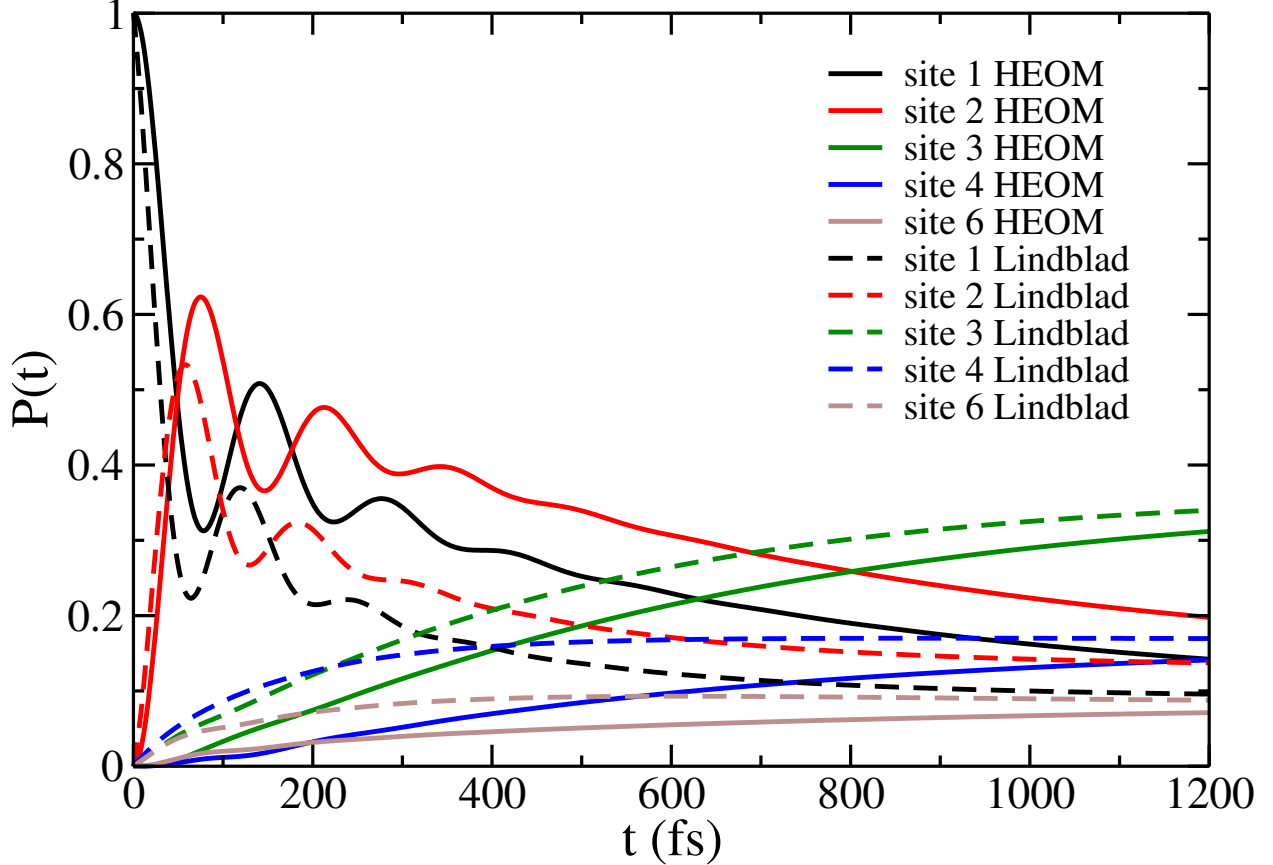


Figure 6: Population dynamics of different sites in the FMO complex at 300 K with Debye spectral density. All parameters are defined in section 4.2, and dynamics are obtained using numerically exact HEOM (solid lines) and the Lindblad equation (dashed lines). The population is initialized at site 1.

to the molecular triad case where  $\eta \gg V$ ). However, the deviations between the Lindblad and HEOM results are rather large, with the former exhibiting faster short-time and slower long-time dynamics, as evidenced by the shallower slope of  $P(t)$  for Lindblad results after  $t = 600$  fs. This outcome is consistent with the general trends shown in Figure 4.

### 5.3 Quantum Circuit Simulation Results

In this section, we report results obtained by applying the qHEOM algorithm described in Section 2 to simulate the charge and energy transfer dynamics in the two model systems under consideration on quantum circuits. Figure 7 compares results obtained via qHEOM

to results obtained via HEOM on a classical computer. The qHEOM results were obtained by utilizing IBM’s noisy quantum circuit simulator, QasmSimulator from the Qiskit Aer package,<sup>129</sup> sampling 20000 shots per time point. Figure 7(a) shows the dynamics of the  $\pi\pi^*$  population in CPC<sub>60</sub> based on the projection operator in eq 29 which treats the full reduced electronic density matrix as the quantity of interest (*i.e.* projects onto the subspace  $S = \{DD, DA, AD, AA\}$ ) and yields a 3-qubit circuit (with dilation). Figure 7(b) shows the energy transfer dynamics in the FMO complex, where we measure populations at sites 1, 2, 3, and 6 (*i.e.* the subspace  $S = \{11, 22, 33, 66\}$ ), capturing the primary excitation pathway  $1 \rightarrow 2 \rightarrow 3$ .<sup>73,117,130</sup>

The excellent agreement between the qHEOM and HEOM results validates the accuracy of our quantum algorithm, as well as its ability to simulate non-unitary dynamics of open quantum systems on a unitary circuit. It also demonstrates the ability of qHEOM to accurately simulate non-Markovian dynamics beyond the range of applicability of the Lindblad quantum master equation.

Next, we report the results obtained via qHEOM on NISQ devices. Figure 8 shows the charge transfer dynamics in CPC<sub>60</sub> as obtained by running qHEOM on the IBM Sherbrooke quantum computer, with the same projected subspace  $S = \{DD, DA, AD, AA\}$  as in Figure 7(a). Populations for the donor  $\pi\pi^*$  state [ $P_D(t)$ ] and the acceptor CT1 state [ $P_A(t)$ ] were measured at 40 time points, each corresponding to an individual circuit sampled 20000 times. Dynamic decoupling (XX sequence) and 2-qubit Clifford gate twirling error mitigation techniques were used within Qiskit. Circuit complexity remains consistent across time points, with an example circuit depth of 60 and 11 2-qubit gates shown in Supporting Information (SI).

Inspection of Figure 8 reveals that while simulation on the NISQ device can reproduce the general dynamical behavior, noise gives rise to discrepancies compared with the exact results. These discrepancies exhibit notable patterns. First, larger errors occur when  $P_D(t)$  or  $P_A(t)$  approaches 0 (as the other population nears 1), particularly in the short-time region for the

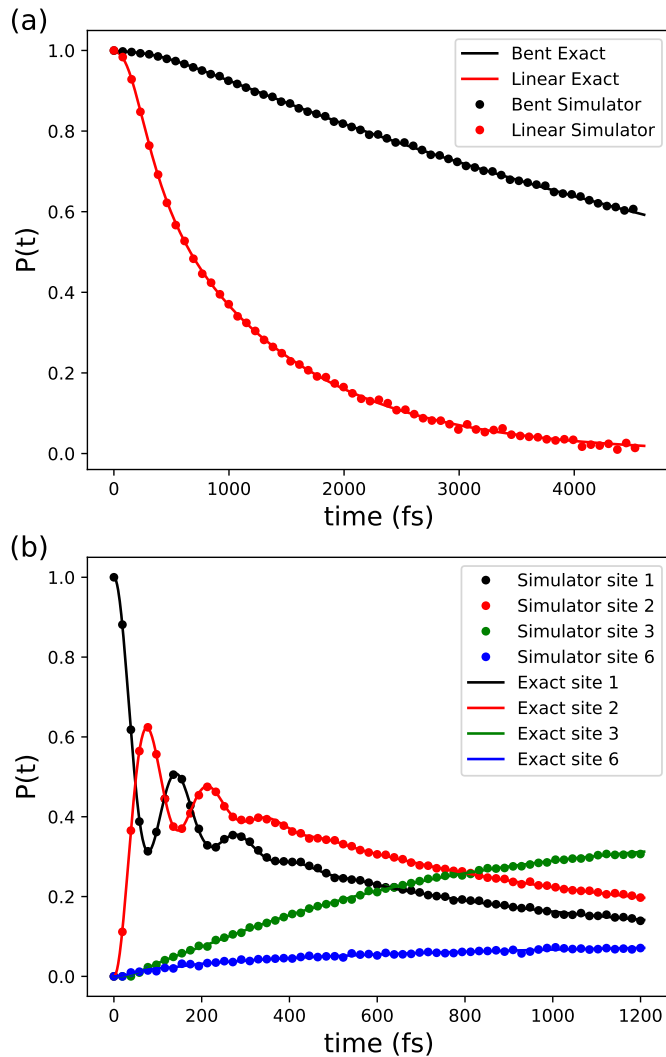


Figure 7: Quantum circuit simulation of (a)  $\pi\pi^*$  state population dynamics of the  $\text{CPC}_{60}$  molecular triad in tetrahydrofuran and (b) population dynamics of different sites in the FMO complex. The solid lines, labeled “Exact”, correspond to HEOM results from Figures 5 and 6. Dotted points show quantum circuit results obtained via IBM QasmSimulator (Qiskit Aer<sup>129</sup>), with 20000 shots per time point.

bent conformation and across short- and long-time regions for the linear conformation. This behavior is consistent with observations from previous studies,<sup>35,62</sup> which reported larger deviations in NISQ results at early times when the exact population of certain states is close to zero. Second, deviations are more pronounced when the exact population is near 0, compared to when it is near 1. In particular,  $P_A(t)$  exhibits larger errors than  $P_D(t)$  at short

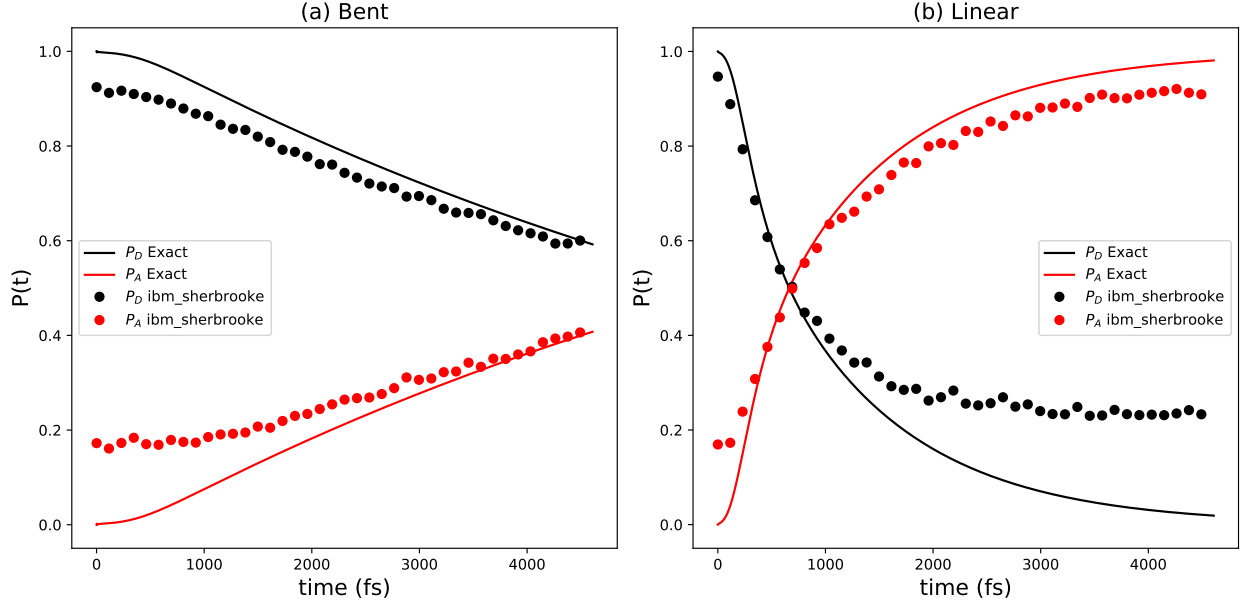


Figure 8: Population dynamics of the  $\text{CPC}_{60}$  molecular triad: (a) Bent conformation, (b) Linear conformation.  $P_D$  represents the population in the  $\pi\pi^*$  (donor) state, and  $P_A$  represents the population in the CT1 (acceptor) state, with the projection subspace  $S = \{DD, DA, AD, AA\}$ . Solid lines show the exact HEOM results, while scatter points indicate quantum circuit results obtained from the IBM Sherbrooke quantum computer. Each time point was sampled with 20000 shots. Error mitigation techniques, including dynamic decoupling (XX sequence) and 2-qubit Clifford gate twirling, were applied using Qiskit.

times for the bent conformation, and  $P_D(t)$  shows greater errors than  $P_A(t)$  at longer times for the linear conformation. This effect is attributed to noise in the sampling measurements.

To explain this trend, we note that after running the circuit in Figure 1, the population for  $|i\rangle$  with  $ii \in S$  is retrieved by counting instances of  $|\tilde{i}i\mathbf{0}\rangle$  with the ancilla qubit in  $|0\rangle$ . If  $N_i$  counts occur from  $N_c$  total measurements, the population of state  $|i\rangle$  is calculated as

$$P_i = \sigma_0 \sqrt{N_i/N_c} \ , \quad (47)$$

where  $\sigma_0$  is the largest singular value of the propagator (see eq 3). Allowing for noise in  $N_i$ ,  $N_i = N_{exact} \pm N_{err}$ , the error in  $P_i$  can be estimated as follows:

$$P_i = \sigma_0 \sqrt{N_i/N_c} = P_{exact} (\sqrt{1 \pm N_{err}/N_{exact}}) \ . \quad (48)$$

Thus, as  $P_{exact}$  approaches 0,  $N_{exact}$  is small, increasing the deviation of  $(\sqrt{1 \pm N_{err}/N_{exact}})$  from 1.

Importantly, error mitigation does reduce deviations significantly, with results in the SI showing that the unmitigated NISQ data exhibits the same trends but with larger errors. The results in Figure 8 surpass in accuracy previously reported results obtained on 3-qubit circuits in Ref. 62, where the Sz.-Nagy dilation method was employed to handle the non-unitary propagator  $G(t)$ . Here, SVD dilation with an efficient Walsh operator representation of  $U_\Sigma$  reduced circuit depth, as shown in Table 3. Thus, combining SVD dilation with Walsh operator implementation for  $U_\Sigma$  reduces circuit complexity by more than a factor of 2 compared to the Sz.-Nagy approach.

Table 3: Circuit complexity for different dilation methods. ‘‘SVD’’ refers to the SVD dilation approach shown in Figure 1, where the diagonal unitary operator  $U_\Sigma$  is directly compiled, while ‘‘SVD+Walsh’’ indicates the SVD dilation approach combined with the Walsh operator representation for  $U_\Sigma$ . The dilation is based on the propagator  $G(t)$  at  $t = 2073.5$  fs for the linear conformation shown in Figure 8. Circuits are compiled to the basis gate set of the IBM Sherbrooke quantum computer ( $X$ ,  $\sqrt{X}$ ,  $R_z$ , and ECR) and adapted to its specific topology. The 2-qubit gate count reflects the number of ECR gates in the circuit.

Dilation method	Sz.-Nagy	SVD	SVD + Walsh
Depth	148	105	60
Number of 2-qubit gate	28	22	11

Figure 9 shows the population dynamics of FMO obtained by running qHEOM on the IBM Sherbrooke quantum computer. The projection subspace  $S = \{11, 22, 33, 66\}$  is consistent with Figure 7(b). Each quantum circuit was sampled 20000 times with error mitigation applied. Circuit complexity is uniform across time points (an example is provided in Table 4), and a sample circuit diagram is available in the SI.

Overall, the NISQ device accurately simulates the energy transfer dynamics in FMO, capturing both the coherent oscillations between site 1 and site 2 at short times and the

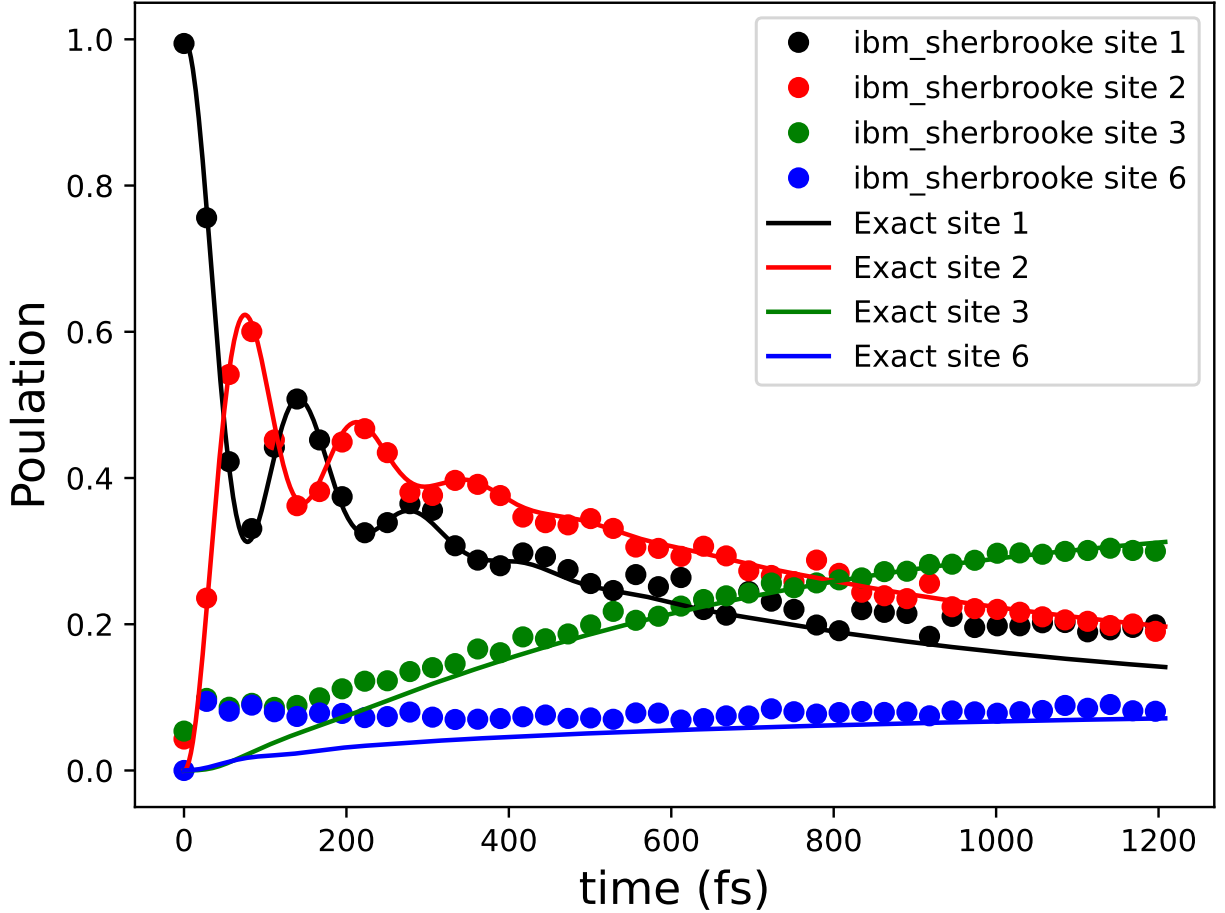


Figure 9: Population dynamics of the FMO complex. Solid lines indicate the exact HEOM simulation results, while dotted scatter points represent quantum circuit results from the IBM Sherbrooke quantum computer. Each time point was sampled with 20000 shots. The projection subspace is defined as  $S = \{11, 22, 33, 66\}$ . Dynamic decoupling (XX sequence) and 2-qubit Clifford gate twirling error mitigation techniques were applied using Qiskit.

growth of population at site 3 at longer times (the terminal site<sup>117</sup>). Similar to the observations in Figure 8, slight deviations in NISQ results appear when  $P(t)$  approaches zero, particularly in the initial populations of sites 3 and 6, and in the long-term population of site 1.

In both Figure 8 and Figure 9, the projected subspace  $S$  includes four states, resulting in a nearly identical depth for the 3-qubit circuits in both cases. However, compared to the CPC<sub>60</sub> results in Figure 8, the NISQ results for the FMO complex are more accurate. This is because,

in the FMO case, the largest singular value  $\sigma_0$  of  $G(t)$  in eq 3 is less than 1, whereas, for  $\text{CPC}_{60}$ ,  $\sigma_0$  exceeds 1. For the same  $P_{exact}$  in eq 48, we have  $N_{exact} = N_c(P_{exact}/\sigma_0)^2$ . A smaller  $\sigma_0$  thus results in a larger  $N_{exact}$ , reducing the deviation of the error factor  $(\sqrt{1 \pm N_{err}/N_{exact}})$  from 1.

The quantum algorithm based on the dilation of  $G(t)$  used in this work has the advantage of allowing the selection of projection subspace towards reducing the circuit depth, thereby lowering the effect of noise.<sup>62</sup> Figure 10 shows the population dynamics of the molecular triad obtained using the IBM Sherbrooke quantum computer, where the projected subspace is restricted to  $S = \{DD, AA\}$ . In this case, the corresponding dilation circuit involves only 2 qubits, with examples of the circuit shown in the SI. As shown in the figure, compared to Figure 8, the accuracy of the NISQ results has improved significantly. For both conformations, the NISQ results closely match the exact results, with only minor deviations when the exact population approaches zero. The reasons for these errors are the same as discussed earlier in Figure 8 and Figure 9. The improved accuracy of the NISQ results is attributed to the significant reduction in circuit depth: in Table 4, due to the decrease in the number of qubits, the example circuit depth is reduced from 60 to 15, and the number of 2-qubit gates decreases from 11 to 2.

Table 4: Circuit complexities for different examples from Figure 8 to Figure 11. As specific cases, the circuit for  $\text{CPC}_{60}$  uses the propagator for the linear conformation at  $t = 2073.5$  fs, while for FMO uses the propagator at  $t = 612.0$  fs. The 3-qubit  $\text{CPC}_{60}$  and 3-qubit FMO correspond to projection subspaces  $S = \{DD, DA, AD, AA\}$  and  $S = \{11, 22, 33, 66\}$ , respectively, while the 2-qubit  $\text{CPC}_{60}$  and 2-qubit FMO correspond to  $S = \{DD, AA\}$  and  $S = \{11, 22\}$ , respectively. The circuit compilation settings are the same as those in Table 3.

	Depth	Number of 2-qubit gates
3 qubits $\text{CPC}_{60}$	60	11
3 qubits FMO	67	12
2 qubits $\text{CPC}_{60}$	15	2
2 qubits FMO	17	2

The same approach can be applied to the FMO complex. It is important to note that



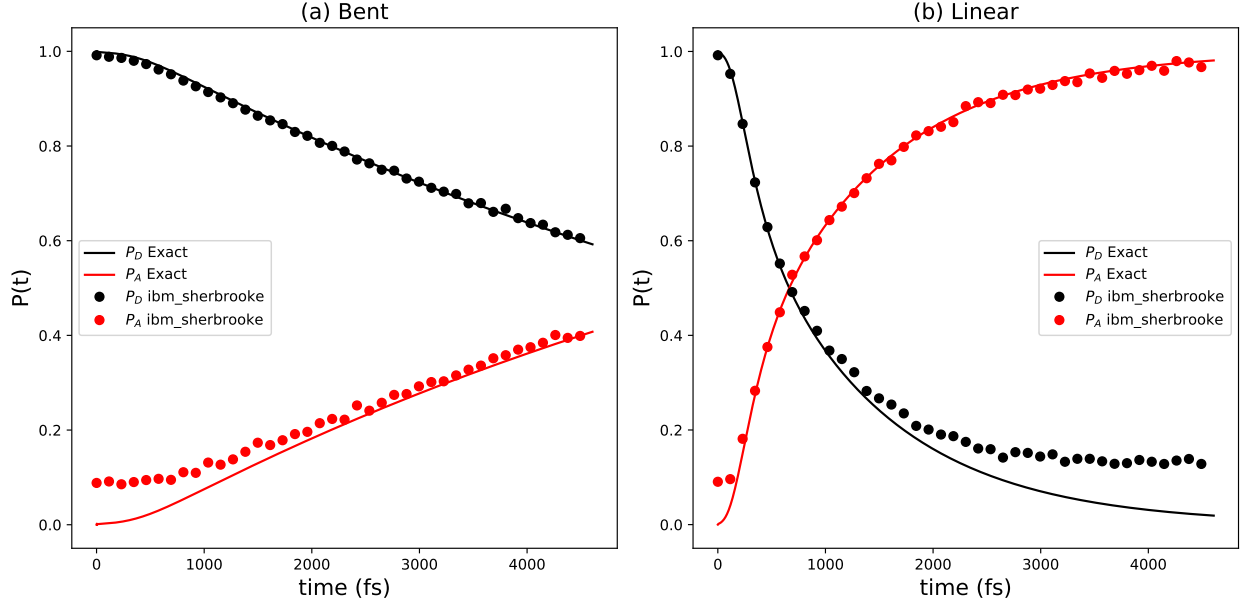


Figure 10: Population dynamics of the  $\text{CPC}_{60}$  molecular triad. The projection subspace is defined as  $S = \{DD, AA\}$ , yielding 2-qubit quantum circuits. Solid lines denote the exact HEOM simulation results, while scatter points represent quantum circuit results from the IBM Sherbrooke quantum computer. Each time point was sampled with 20000 shots, with error mitigation applied.

the projection operator in eq 29 should satisfy  $\mathcal{P}|\Psi(t = 0)\rangle = |\Psi(t = 0)\rangle$ , meaning that the projection subspace must include the initial site  $|1\rangle$ . For the 2-qubit circuit,  $S$  should take the form of  $\{11, ij\}$ . Therefore, to measure the populations of sites 1, 2, 3, and 6 at a given time, we need three 2-qubit circuits corresponding to the projection subspaces  $S_1 = \{11, 22\}$ ,  $S_2 = \{11, 33\}$ , and  $S_3 = \{11, 66\}$ . The decomposition of the projection subspace can significantly reduce the circuit depth. As an example shown in Table 4, after decomposing the  $S = \{11, 22, 33, 66\}$  into  $S_1$ ,  $S_2$ , and  $S_3$ , the circuit with a depth of 67 and 12 two-qubit gates is transformed into three circuits, each with a depth of around 17 and containing two two-qubit gates.

The reduction in circuit complexity has significantly improved the accuracy of the NISQ results. Figure 11 shows the IBM Sherbrooke results for the FMO complex, where we use  $S_1 = \{11, 22\}$ ,  $S_2 = \{11, 33\}$ , and  $S_3 = \{11, 66\}$  to construct 2-qubit quantum circuits. Except for slight deviations in the population of sites 3 and 6 at early time points  $t < 200$  fs,

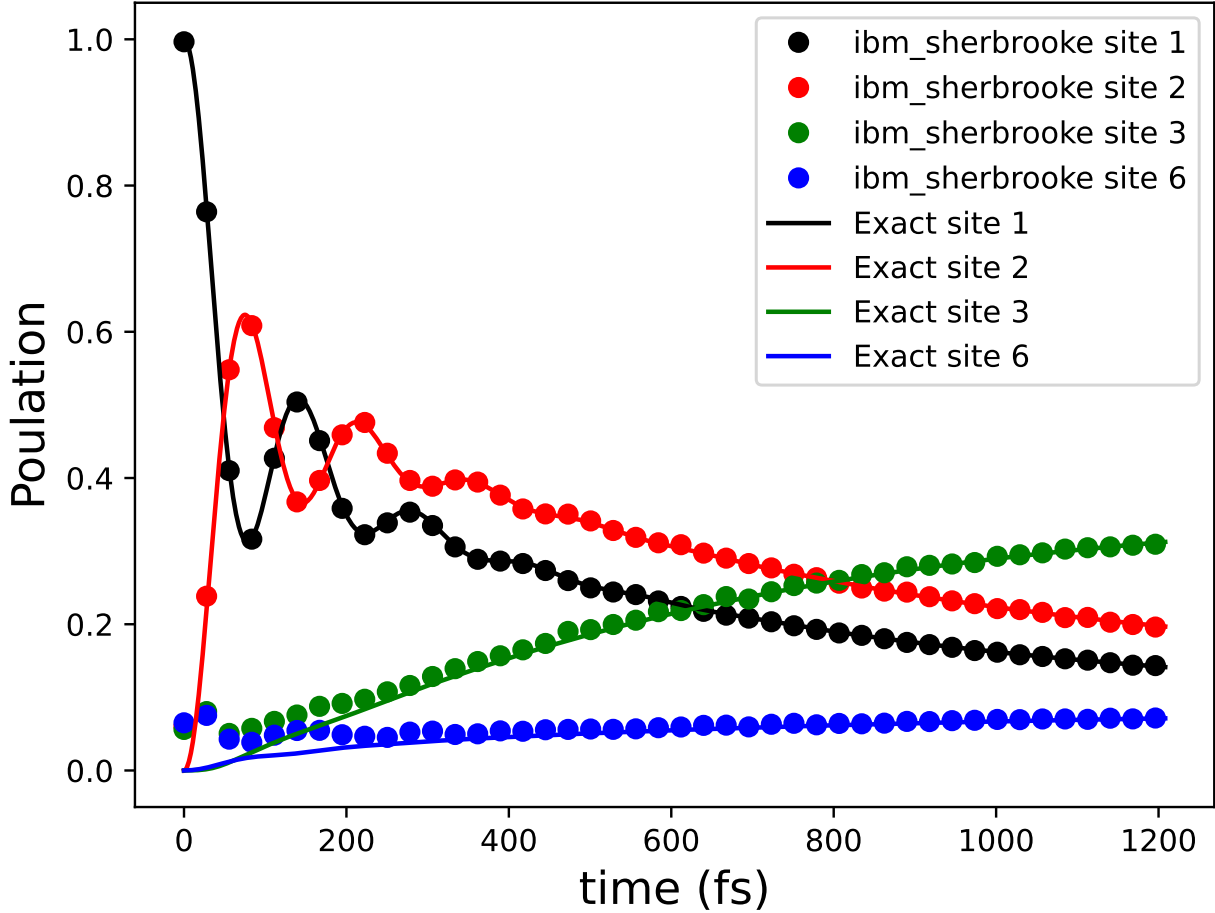


Figure 11: Population dynamics of the FMO complex. The solid lines represent the exact HEOM results, and the dot scatter points represent the quantum circuit results from the IBM Sherbrooke quantum computer. To calculate the populations of states  $|1\rangle$ ,  $|2\rangle$ ,  $|3\rangle$ , and  $|6\rangle$  using two-qubit circuits, three different projection subspaces are employed:  $S_1 = \{11, 22\}$ ,  $S_2 = \{11, 33\}$ , and  $S_3 = \{11, 66\}$ . Each time point is measured by 20000 shots with error mitigation.

the IBM Sherbrooke results align almost perfectly with the exact results. This demonstrates that our quantum algorithm can achieve high precision in simulating the population dynamics of the FMO complex on actual NISQ devices.

## 6 Concluding Remarks

We have introduced the qHEOM quantum algorithm and demonstrated its accuracy and practical utility by using it to simulate charge transfer in a solvated molecular triad and excitation energy transfer in the FMO complex, on NISQ devices. We have shown that the dynamics in both cases are non-Markovian and beyond the weak system-bath coupling limit, thereby rendering a description via the Lindblad quantum master equation inadequate. Specifically, we found that the Lindblad master equation is limited to the coherent dynamics regime, fails to capture the charge transfer rate in the molecular triad, and provides only qualitative results for energy transfer in FMO.

qHEOM implements the SVD dilation to convert the non-unitary HEOM propagator into unitary gates and utilizes the Walsh operator representation to efficiently represent the diagonal unitary operator within the dilation circuit. In doing so, qHEOM significantly reduces circuit complexity compared to algorithms based on Sz.-Nagy dilation.<sup>18,62</sup> Further reduction in circuit depth and complexity is achieved by projecting the HEOM propagator onto the subspace of quantities of interest. Since different subspaces are independent, this approach also allows for parallel quantum computing implementations on multiple circuits.

Our qHEOM simulations performed on the IBM NISQ device show that device noise can lead to significant discrepancies. The discrepancy is found to be related to the properties of the propagator. When the largest singular value of the propagator is relatively large, it can amplify this discrepancy. Consequently, for circuits of similar complexity, the NISQ results for energy transfer in the FMO complex are more accurate than those for charge transfer in the molecular triad.

Reducing the size of the projection subspace can mitigate device-induced errors. By limiting the projection subspace to include only two states, the IBM device achieved highly accurate quantitative results. Notably, for energy transfer in the FMO complex, the NISQ results are almost perfectly aligned with numerically exact benchmark results.

When simulating open quantum system dynamics via qHEOM on IBM quantum com-

puters, error mitigation techniques included in Qiskit can effectively reduce errors caused by device noise. Future work could explore alternative methods to further reduce noise, such as using different dynamic decoupling sequences,<sup>131–134</sup> increasing the number of qubits to mitigate errors,<sup>135,136</sup> and integrating quantum error correction techniques with machine learning approaches.<sup>137,138</sup>

We note that the quantum algorithm implemented in this work is quite general. Although we used it to implement the HEOM propagator, the same algorithm could be applied to implement propagators from other quantum master equations. Those propagators could be obtained using various numerical methods, such as TT-TFD,<sup>15–17</sup> path integral,<sup>27–35</sup> time-evolving matrix product operator (TEMPO),<sup>139–141</sup> GQME,<sup>13,17,36–47</sup> and others. Once the propagator for the evolution of the system is obtained, the SVD dilation and Walsh operator representation implemented in this work can be applied to construct the corresponding quantum circuit.

In future studies, we will use bosonic quantum devices to simulate the dissipative dynamics of chemical systems according to the quantum algorithm developed in this work. Hybrid qubit-qumode quantum devices could offer significant advantages over traditional qubit-based quantum platforms,<sup>142–146</sup> particularly for implementations of the HEOM methodology where the degrees of freedom of the environment are decomposed into several effective bosonic modes.

## 7 Acknowledgments

Xiaohan Dan acknowledges Professor Qiang Shi, Professor Chen Wang, Ningyi Lyu, Delmar G. A. Cabral, Brandon Allen, and Yuanjun Shi for useful discussions and assistance with illustrations. VSB acknowledges support from the National Science Foundation Engines Development Award: Advancing Quantum Technologies (CT) under Award Number 2302908, and partial support from the National Science Foundation Center for Quantum Dynamics on

Modular Quantum Devices (CQD-MQD) under Award Number 2124511. E.G. acknowledges additional support from the NSF Grant No. CHE 2154114. VSB acknowledges a generous allocation of HPC time from NERSC and from the Yale Center for Research Computing.

## **Supporting Information Available**

Includes a detailed description of the quantum circuits and additional figures.

## **8 Code availability**

The Python code for qHEOM simulations is available at <https://github.com/XiaohanDan97/qHEOM>.

## References

- (1) Breuer, H. P.; Petruccione, F. *The Theory of Open Quantum Systems*; Oxford University Press: New York, 2002.
- (2) Nitzan, A. *Chemical Dynamics in Condensed Phases*; Oxford University Press: New York, 2006.
- (3) Weiss, U. *Quantum Dissipative Systems*, 4th ed.; World Scientific: New Jersey, 2012.
- (4) Wangsness, R. K.; Bloch, F. The dynamical theory of nuclear induction. *Phys. Rev.* **1953**, *89*, 728.
- (5) Redfield, A. G. On the theory of relaxation processes. *IBM J. Res.* **1957**, *1*, 19.
- (6) Pollard, W. T.; Felts, A. K.; Friesner, R. A. The Redfield equation in condensed-phase quantum dynamics. *Adv. Chem. Phys.* **1996**, *93*, 77.
- (7) Carmichael, H. J. *Statistical methods in quantum optics 1: master equations and Fokker-Planck equations*; Springer Science & Business Media, 2013.
- (8) Manzano, D. A short introduction to the Lindblad master equation. *AIP Adv.* **2020**, *10*, 025106.
- (9) Alicki, R.; Lendi, K. *Quantum Dynamical Semigroups and Applications*; Springer-Verlag: Berlin, 1987.
- (10) Zheng, X.; Yan, Y.; Di Ventra, M. Kondo Memory in Driven Strongly Correlated Quantum Dots. *Phys. Rev. Lett.* **2013**, *111*, 086601.
- (11) Breuer, H.-P.; Laine, E.-M.; Piilo, J.; Vacchini, B. Colloquium: Non-Markovian dynamics in open quantum systems. *Rev. Mod. Phys.* **2016**, *88*, 021002.
- (12) de Vega, I.; Alonso, D. Dynamics of non-Markovian open quantum systems. *Rev. Mod. Phys.* **2017**, *89*, 015001.

- (13) Dan, X.; Xu, M.; Yan, Y.; Shi, Q. Generalized master equation for charge transport in a molecular junction: Exact memory kernels and their high order expansion. *J. Chem. Phys.* **2022**, *156*, 134114.
- (14) Dan, X.; Xu, M.; Stockburger, J. T.; Ankerhold, J.; Shi, Q. Efficient low-temperature simulations for fermionic reservoirs with the hierarchical equations of motion method: Application to the Anderson impurity model. *Phys. Rev. B* **2023**, *107*, 195429.
- (15) Gelin, M. F.; Borrelli, R. Thermal Schrödinger Equation: Efficient Tool for Simulation of Many-Body Quantum Dynamics at Finite Temperature. *Annalen der Physik* **2017**, *529*, 1700200.
- (16) Borrelli, R.; Gelin, M. F. Finite temperature quantum dynamics of complex systems: Integrating thermo-field theories and tensor-train methods. *WIREs Computational Molecular Science* **2021**, *11*, e1539.
- (17) Lyu, N.; Mulvihill, E.; Soley, M. B.; Geva, E.; Batista, V. S. Tensor-Train Thermo-Field Memory Kernels for Generalized Quantum Master Equations. *J. Chem. Theory Comput.* **2023**, *19*, 1111–1129.
- (18) Lyu, N.; Khazaei, P.; Geva, E.; Batista, V. S. Simulating Cavity-Modified Electron Transfer Dynamics on NISQ Computers. *J. Phys. Chem. Lett.* **2024**, *15*, 9535–9542.
- (19) Tanimura, Y.; Kubo, R. Time Evolution of a Quantum System in Contact with a Nearly Gaussian-Markoffian Noise Bath. *J. Phys. Soc. Jpn.* **1989**, *58*, 101–114.
- (20) Tanimura, Y. Stochastic Liouville, Langevin, Fokker–Planck, and Master Equation Approaches to Quantum Dissipative Systems. *J. Phys. Soc. Jpn.* **2006**, *75*, 082001.
- (21) Tanimura, Y. Numerically “Exact” Approach to Open Quantum Dynamics: The Hierarchical Equations of Motion (HEOM). *J. Chem. Phys.* **2020**, *153*, 020901.

- (22) Shi, Q.; Chen, L.-P.; Nan, G.-J.; Xu, R.-X.; Yan, Y.-J. Electron Transfer Dynamics: Zusman Equation Versus Exact Theory. *J. Chem. Phys.* **2009**, *130*, 164518.
- (23) Shi, Q.; Xu, Y.; Yan, Y.; Xu, M. Efficient propagation of the hierarchical equations of motion using the matrix product state method. *J. Chem. Phys.* **2018**, *148*, 174102.
- (24) Dan, X.; Shi, Q. Theoretical study of nonadiabatic hydrogen atom scattering dynamics on metal surfaces using the hierarchical equations of motion method. *J. Chem. Phys.* **2023**, *159*, 044101.
- (25) Wang, H.; Thoss, M. Multilayer Formulation of the Multiconfiguration Time-dependent Hartree Theory. *J. Chem. Phys.* **2003**, *119*, 1289–1299.
- (26) Wang, H. Multilayer Multiconfiguration Time-Dependent Hartree Theory. *J. Phys. Chem. A* **2015**, *119*, 7951–7965.
- (27) Topaler, M.; Makri, N. System-specific discrete variable representations for path integral calculations with quasi-adiabatic propagators. *Chem. Phys. Lett.* **1993**, *210*, 448–457.
- (28) Makri, N. Numerical path integral techniques for long time dynamics of quantum dissipative systems. *J. Math. Phys.* **1995**, *36*, 2430–2457.
- (29) Weiss, S.; Eckel, J.; Thorwart, M.; Egger, R. Iterative real-time path integral approach to nonequilibrium quantum transport. *Phys. Rev. B* **2008**, *77*, 195316.
- (30) Segal, D.; Millis, A. J.; Reichman, D. R. Numerically exact path-integral simulation of nonequilibrium quantum transport and dissipation. *Phys. Rev. B* **2010**, *82*, 205323.
- (31) Weiss, S.; Hütten, R.; Becker, D.; Eckel, J.; Egger, R.; Thorwart, M. Iterative path integral summation for nonequilibrium quantum transport. *Phys. Status Solidi B* **2013**, *250*, 2298–2314.



- (32) Makri, N. Small Matrix Path Integral for System-Bath Dynamics. *J. Chem. Theory Comput.* **2020**, *16*, 4038–4049.
- (33) Bose, A.; Walters, P. L. A multisite decomposition of the tensor network path integrals. *J. Chem. Phys.* **2022**, *156*, 024101.
- (34) Walters, P. L.; Wang, F. Path integral quantum algorithm for simulating non-Markovian quantum dynamics in open quantum systems. *Phys. Rev. Res.* **2024**, *6*, 013135.
- (35) Seneviratne, A.; Walters, P. L.; Wang, F. Exact Non-Markovian Quantum Dynamics on the NISQ Device Using Kraus Operators. *ACS Omega* **2024**, *9*, 9666–9675.
- (36) Zwanzig, R. Memory Effects in Irreversible Thermodynamics. *Phys. Rev.* **1961**, *124*, 983–992.
- (37) Shi, Q.; Geva, E. A new approach to calculating the memory kernel of the generalized quantum master equation for an arbitrary system-bath coupling. *J. Chem. Phys.* **2003**, *119*, 12063.
- (38) Shi, Q.; Geva, E. A Semiclassical Generalized Quantum Master Equation for an Arbitrary System-Bath Coupling. *J. Chem. Phys.* **2004**, *120*, 10647–10658.
- (39) Zhang, M.-L.; Ka, B. J.; Geva, E. Nonequilibrium quantum dynamics in the condensed phase via the generalized quantum master equation. *J. Chem. Phys.* **2006**, *125*, 044106.
- (40) Kelly, A.; Montoya-Castillo, A.; Wang, L.; Markland, T. E. Generalized quantum master equations in and out of equilibrium: When can one win? *J. Chem. Phys.* **2016**, *144*, 184105.
- (41) Montoya-Castillo, A.; Reichman, D. R. Approximate but accurate quantum dynamics

- from the Mori formalism: I. Nonequilibrium dynamics. *J. Chem. Phys.* **2016**, *144*, 184104.
- (42) Montoya-Castillo, A.; Reichman, D. R. Approximate but accurate quantum dynamics from the Mori formalism. II. Equilibrium time correlation functions. *J. Chem. Phys.* **2017**, *146*, 084110.
- (43) Pfalzgraff, W. C.; Montoya-Castillo, A.; Kelly, A.; Markland, T. E. Efficient construction of generalized master equation memory kernels for multi-state systems from nonadiabatic quantum-classical dynamics. *J. Chem. Phys.* **2019**, *150*, 244109.
- (44) Mulvihill, E.; Gao, X.; Liu, Y.; Schubert, A.; Dunietz, B. D.; Geva, E. Combining the mapping Hamiltonian linearized semiclassical approach with the generalized quantum master equation to simulate electronically nonadiabatic molecular dynamics. *J. Chem. Phys.* **2019**, *151*, 074103.
- (45) Mulvihill, E.; Lenn, K. M.; Gao, X.; Schubert, A.; Dunietz, B. D.; Geva, E. Simulating energy transfer dynamics in the Fenna–Matthews–Olson complex via the modified generalized quantum master equation. *J. Chem. Phys.* **2021**, *154*, 204109.
- (46) Mulvihill, E.; Geva, E. Simulating the dynamics of electronic observables via reduced-dimensionality generalized quantum master equations. *J. Chem. Phys.* **2022**, *156*, 044119.
- (47) Ng, N.; Limmer, D. T.; Rabani, E. Nonuniqueness of generalized quantum master equations for a single observable. *J. Chem. Phys.* **2021**, *155*, 156101.
- (48) Nielsen, M. A.; Chuang, I. *Quantum computation and quantum information*; Cambridge University Press: Cambridge, 2010.
- (49) Kassal, I.; Whitfield, J. D.; Perdomo-Ortiz, A.; Yung, M.-H.; Aspuru-Guzik, A. Sim-

- ulating Chemistry Using Quantum Computers. *Annu. Rev. Phys. Chem.* **2011**, *62*, 185–207.
- (50) Georgescu, I. M.; Ashhab, S.; Nori, F. Quantum simulation. *Rev. Mod. Phys.* **2014**, *86*, 153–185.
- (51) Cao, Y.; Romero, J.; Olson, J. P.; Degroote, M.; Johnson, P. D.; Kieferová, M.; Kivlichan, I. D.; Menke, T.; Peropadre, B.; Sawaya, N. P. D.; Sim, S.; Veis, L.; Aspuru-Guzik, A. Quantum Chemistry in the Age of Quantum Computing. *Chem. Rev.* **2019**, *119*, 10856–10915.
- (52) Ollitrault, P. J.; Miessen, A.; Tavernelli, I. Molecular Quantum Dynamics: A Quantum Computing Perspective. *Acc. Chem. Res.* **2021**, *54*, 4229–4238.
- (53) Wiebe, N.; Berry, D. W.; Høyer, P.; Sanders, B. C. Simulating quantum dynamics on a quantum computer. *J. Phys. A: Math. Theor.* **2011**, *44*, 445308.
- (54) Yao, Y.-X.; Gomes, N.; Zhang, F.; Wang, C.-Z.; Ho, K.-M.; Iadecola, T.; Orth, P. P. Adaptive Variational Quantum Dynamics Simulations. *PRX Quantum* **2021**, *2*, 030307.
- (55) Sweke, R.; Sinayskiy, I.; Bernard, D.; Petruccione, F. Universal simulation of Markovian open quantum systems. *Phys. Rev. A* **2015**, *91*, 062308.
- (56) Hu, Z.; Xia, R.; Kais, S. A quantum algorithm for evolving open quantum dynamics on quantum computing devices. *Sci. Rep.* **2020**, *10*, 3301.
- (57) Schlimgen, A. W.; Head-Marsden, K.; Sager, L. M.; Narang, P.; Mazziotti, D. A. Quantum Simulation of Open Quantum Systems Using a Unitary Decomposition of Operators. *Phys. Rev. Lett.* **2021**, *127*, 270503.
- (58) Schlimgen, A. W.; Head-Marsden, K.; Sager, L. M.; Narang, P.; Mazziotti, D. A.

- Quantum simulation of the Lindblad equation using a unitary decomposition of operators. *Phys. Rev. Res.* **2022**, *4*, 023216.
- (59) Li, X.; Lyu, S.-X.; Wang, Y.; Xu, R.-X.; Zheng, X.; Yan, Y. Toward quantum simulation of non-Markovian open quantum dynamics: A universal and compact theory. *Phys. Rev. A* **2024**, *110*, 032620.
- (60) Head-Marsden, K.; Krastanov, S.; Mazziotti, D. A.; Narang, P. Capturing non-Markovian dynamics on near-term quantum computers. *Phys. Rev. Res.* **2021**, *3*, 013182.
- (61) Schlimgen, A. W.; Head-Marsden, K.; Sager-Smith, L. M.; Narang, P.; Mazziotti, D. A. Quantum state preparation and nonunitary evolution with diagonal operators. *Phys. Rev. A* **2022**, *106*, 022414.
- (62) Wang, Y.; Mulvihill, E.; Hu, Z.; Lyu, N.; Shivpuje, S.; Liu, Y.; Soley, M. B.; Geva, E.; Batista, V. S.; Kais, S. Simulating Open Quantum System Dynamics on NISQ Computers with Generalized Quantum Master Equations. *J. Chem. Theory Comput.* **2023**, *19*, 4851–4862.
- (63) McArdle, S.; Jones, T.; Endo, S.; Li, Y.; Benjamin, S. C.; Yuan, X. Variational ansatz-based quantum simulation of imaginary time evolution. *npj Quantum Inf.* **2019**, *5*, 75.
- (64) Motta, M.; Sun, C.; Tan, A. T.; O’Rourke, M. J.; Ye, E.; Minnich, A. J.; Brandao, F. G.; Chan, G. K.-L. Determining eigenstates and thermal states on a quantum computer using quantum imaginary time evolution. *Nat. Phys.* **2020**, *16*, 205–210.
- (65) Kamakari, H.; Sun, S.-N.; Motta, M.; Minnich, A. J. Digital Quantum Simulation of Open Quantum Systems Using Quantum Imaginary–Time Evolution. *PRX Quantum* **2022**, *3*, 010320.

- (66) Li, Y.; Benjamin, S. C. Efficient variational quantum simulator incorporating active error minimization. *Phys. Rev. X* **2017**, *7*, 021050.
- (67) Chen, M.-C.; Gong, M.; Xu, X.; Yuan, X.; Wang, J.-W.; Wang, C.; Ying, C.; Lin, J.; Xu, Y.; Wu, Y.; others Demonstration of adiabatic variational quantum computing with a superconducting quantum coprocessor. *Phys. Rev. Lett.* **2020**, *125*, 180501.
- (68) Endo, S.; Sun, J.; Li, Y.; Benjamin, S. C.; Yuan, X. Variational Quantum Simulation of General Processes. *Phys. Rev. Lett.* **2020**, *125*, 010501.
- (69) Lee, C.-K.; Hsieh, C.-Y.; Zhang, S.; Shi, L. Variational quantum simulation of chemical dynamics with quantum computers. *J. Chem. Theory Comput.* **2022**, *18*, 2105–2113.
- (70) Bacon, D.; Childs, A. M.; Chuang, I. L.; Kempe, J.; Leung, D. W.; Zhou, X. Universal simulation of Markovian quantum dynamics. *Phys. Rev. A* **2001**, *64*, 062302.
- (71) Cleve, R.; Wang, C. Efficient quantum algorithms for simulating Lindblad evolution. *arXiv preprint arXiv:1612.09512* **2016**,
- (72) Luo, J.; Lin, K.; Gao, X. Variational Quantum Simulation of Lindblad Dynamics via Quantum State Diffusion. *J. Phys. Chem. Lett.* **2024**, *15*, 3516–3522.
- (73) Hu, Z.; Head-Marsden, K.; Mazziotti, D. A.; Narang, P.; Kais, S. A general quantum algorithm for open quantum dynamics demonstrated with the Fenna-Matthews-Olson complex. *Quantum* **2022**, *6*, 726.
- (74) Tong, Z.; Gao, X.; Cheung, M. S.; Dunietz, B. D.; Geva, E.; Sun, X. Charge transfer rate constants for the carotenoid-porphyrin-C60 molecular triad dissolved in tetrahydrofuran: The spin-boson model vs the linearized semiclassical approximation. *J. Chem. Phys.* **2020**, *153*, 044105.
- (75) Sweke, R.; Sanz, M.; Sinayskiy, I.; Petruccione, F.; Solano, E. Digital quantum simulation of many-body non-Markovian dynamics. *Phys. Rev. A* **2016**, *94*, 022317.

- (76) Levy, E.; Shalit, O. M. Dilation theory in finite dimensions: The possible, the impossible and the unknown. *Rocky Mountain J. Math.* **2014**, *44*, 203 – 221.
- (77) Welch, J.; Greenbaum, D.; Mostame, S.; Aspuru-Guzik, A. Efficient quantum circuits for diagonal unitaries without ancillas. *New. J. Phys.* **2014**, *16*, 033040.
- (78) Walsh, J. L. A closed set of normal orthogonal functions. *Am. J. Math.* **1923**, *45*, 5–24.
- (79) Schipp, F. *Walsh series. An introduction to dyadic harmonic analysis*; Akadémiai Kiadó, 1990.
- (80) Ishizaki, A.; Fleming, G. R. Unified Treatment of Quantum Coherent and Incoherent Hopping Dynamics in Electronic Energy Transfer: Reduced Hierarchy Equation Approach. *J. Chem. Phys.* **2009**, *130*, 234111.
- (81) Lambert, N.; Raheja, T.; Cross, S.; Menczel, P.; Ahmed, S.; Pitchford, A.; Burgarth, D.; Nori, F. QuTiP-BoFiN: A bosonic and fermionic numerical hierarchical-equations-of-motion library with applications in light-harvesting, quantum control, and single-molecule electronics. *Phys. Rev. Res.* **2023**, *5*, 013181.
- (82) Ke, Y.; Borrelli, R.; Thoss, M. Hierarchical equations of motion approach to hybrid fermionic and bosonic environments: Matrix product state formulation in twin space. *J. Chem. Phys.* **2022**, *156*, 194102.
- (83) Wang, Y.; Yan, Y. Quantum mechanics of open systems: Dissipaton theories. *J. Chem. Phys.* **2022**, *157*, 170901.
- (84) Suzuki, M. Thermo field dynamics in equilibrium and non-equilibrium interacting quantum systems. *J. Phys. Soc. Jpn.* **1985**, *54*, 4483–4485.
- (85) Verstraete, F.; García-Ripoll, J. J.; Cirac, J. I. Matrix Product Density Operators:

- Simulation of Finite-Temperature and Dissipative Systems. *Phys. Rev. Lett.* **2004**, *93*, 207204.
- (86) Feiguin, A. E.; White, S. R. Finite-temperature density matrix renormalization using an enlarged Hilbert space. *Phys. Rev. B* **2005**, *72*, 220401.
- (87) Borrelli, R. Density matrix dynamics in twin-formulation: An efficient methodology based on tensor-train representation of reduced equations of motion. *J. Chem. Phys.* **2019**, *150*, 234102.
- (88) Shi, Q.; Chen, L.; Nan, G.; Xu, R.-X.; Yan, Y. Efficient hierarchical Liouville space propagator to quantum dissipative dynamics. *J. Chem. Phys.* **2009**, *130*, 084105.
- (89) Yan, Y.; Xu, M.; Li, T.; Shi, Q. Efficient propagation of the hierarchical equations of motion using the Tucker and hierarchical Tucker tensors. *J. Chem. Phys.* **2021**, *154*, 194104.
- (90) Ke, Y. Tree tensor network state approach for solving hierarchical equations of motion. *J. Chem. Phys.* **2023**, *158*, 211102.
- (91) Hu, J.; Xu, R.-X.; Yan, Y.-J. Padé Spectrum Decomposition of Fermi Function and Bose Function. *J. Chem. Phys.* **2010**, *133*, 101106.
- (92) Hu, J.; Luo, M.; Jiang, F.; Xu, R.-X.; Yan, Y.-J. Padé Spectrum Decompositions of Quantum Distribution Functions and Optimal Hierarchical Equations of Motion Construction for Quantum Open Systems. *J. Chem. Phys.* **2011**, *134*, 244106.
- (93) Cui, L.; Zhang, H.-D.; Zheng, X.; Xu, R.-X.; Yan, Y. Highly efficient and accurate sum-over-poles expansion of Fermi and Bose functions at near zero temperatures: Fano spectrum decomposition scheme. *J. Chem. Phys.* **2019**, *151*, 024110.

- (94) Zhang, H.-D.; Cui, L.; Gong, H.; Xu, R.-X.; Zheng, X.; Yan, Y. Hierarchical equations of motion method based on Fano spectrum decomposition for low temperature environments. *J. Chem. Phys.* **2020**, *152*, 064107.
- (95) Xu, M.; Yan, Y.; Shi, Q.; Ankerhold, J.; Stockburger, J. T. Taming Quantum Noise for Efficient Low Temperature Simulations of Open Quantum Systems. *Phys. Rev. Lett.* **2022**, *129*, 230601.
- (96) Chen, Z.-H.; Wang, Y.; Zheng, X.; Xu, R.-X.; Yan, Y. Universal time-domain Prony fitting decomposition for optimized hierarchical quantum master equations. *J. Chem. Phys.* **2022**, *156*, 221102.
- (97) Ye, L.; Zhang, H.-D.; Wang, Y.; Zheng, X.; Yan, Y. Low-frequency logarithmic discretization of the reservoir spectrum for improving the efficiency of hierarchical equations of motion approach. *J. Chem. Phys.* **2017**, *147*, 074111.
- (98) Tian, H.; Chen, G.-H. An efficient solution of Liouville-von Neumann equation that is applicable to zero and finite temperatures. *J. Chem. Phys.* **2012**, *137*, 204114.
- (99) Popescu, B.; Rahman, H.; Kleinekathöfer, U. Using the Chebychev expansion in quantum transport calculations. *J. Chem. Phys.* **2015**, *142*, 154103.
- (100) Nakamura, K.; Tanimura, Y. Hierarchical Schrödinger equations of motion for open quantum dynamics. *Phys. Rev. A* **2018**, *98*, 012109.
- (101) Rahman, H.; Kleinekathöfer, U. Chebyshev hierarchical equations of motion for systems with arbitrary spectral densities and temperatures. *J. Chem. Phys.* **2019**, *150*, 244104.
- (102) Tang, Z.; Ouyang, X.; Gong, Z.; Wang, H.; Wu, J. Extended hierarchy equation of motion for the spin-boson model. *J. Chem. Phys.* **2015**, *143*, 224112.



- (103) Ikeda, T.; Scholes, G. D. Generalization of the hierarchical equations of motion theory for efficient calculations with arbitrary correlation functions. *J. Chem. Phys.* **2020**, *152*, 204101.
- (104) Erpenbeck, A.; Hertlein, C.; Schinabeck, C.; Thoss, M. Extending the hierarchical quantum master equation approach to low temperatures and realistic band structures. *J. Chem. Phys.* **2018**, *149*, 064106.
- (105) Mohseni, M.; Rebentrost, P.; Lloyd, S.; Aspuru-Guzik, A. Environment-assisted quantum walks in photosynthetic energy transfer. *J. Chem. Phys.* **2008**, *129*, 174106.
- (106) Breuer, H.-P. Non-Markovian generalization of the Lindblad theory of open quantum systems. *Phys. Rev. A* **2007**, *75*, 022103.
- (107) Ishizaki, A.; Fleming, G. R. Theoretical Examination of Quantum Coherence in a Photosynthetic System at Physiological Temperature. *Proc. Natl. Acad. Sci. USA* **2009**, *106*, 17255.
- (108) Sun, X.; Zhang, P.; Lai, Y.; Williams, K. L.; Cheung, M. S.; Dunietz, B. D.; Geva, E. Computational Study of Charge-Transfer Dynamics in the Carotenoid–Porphyrin–C60 Molecular Triad Solvated in Explicit Tetrahydrofuran and Its Spectroscopic Signature. *J. Phys. Chem. C* **2018**, *122*, 11288–11299.
- (109) Han, J.; Zhang, P.; Aksu, H.; Maiti, B.; Sun, X.; Geva, E.; Dunietz, B. D.; Cheung, M. S. On the Interplay between Electronic Structure and Polarizable Force Fields When Calculating Solution-Phase Charge-Transfer Rates. *J. Chem. Theory Comput.* **2020**, *16*, 6481–6490.
- (110) Hu, Z.; Tong, Z.; Cheung, M. S.; Dunietz, B. D.; Geva, E.; Sun, X. Photoinduced charge transfer dynamics in the carotenoid–porphyrin–C60 triad via the linearized semiclassical nonequilibrium Fermi’s golden rule. *J. Phys. Chem. B* **2020**, *124*, 9579–9591.

- (111) Brian, D.; Liu, Z.; Dunietz, B. D.; Geva, E.; Sun, X. Three-state harmonic models for photoinduced charge transfer. *J. Chem. Phys.* **2021**, *154*, 174105.
- (112) Brian, D.; Sun, X. Charge-Transfer Landscape Manifesting the Structure–Rate Relationship in the Condensed Phase Via Machine Learning. *J. Phys. Chem. B* **2021**, *125*, 13267–13278.
- (113) Brian, D.; Sun, X. Linear-Response and Nonlinear-Response Formulations of the Instantaneous Marcus Theory for Nonequilibrium Photoinduced Charge Transfer. *J. Chem. Theory Comput.* **2021**, *17*, 2065–2079.
- (114) Hu, Z.; Sun, X. All-Atom Nonadiabatic Semiclassical Mapping Dynamics for Photoinduced Charge Transfer of Organic Photovoltaic Molecules in Explicit Solvents. *J. Chem. Theory Comput.* **2022**, *18*, 5819–5836.
- (115) Fenna, R. E.; Matthews, B. W. Chlorophyll arrangement in a bacteriochlorophyll protein from *Chlorobium-Limicola*. *Nature* **1975**, *258*, 573–577.
- (116) Li, Y.-F.; Zhou, W.; Blankenship, R. E.; Allen, J. P. Crystal Structure of The Bacteriochlorophyll a Protein from *Chlorobium Tepidum*. *J. Mol. Biol.* **1997**, *271*, 456.
- (117) Moix, J.; Wu, J.; Huo, P.; Coker, D.; Cao, J. Efficient energy transfer in light-harvesting systems, III: The influence of the eighth bacteriochlorophyll on the dynamics and efficiency in FMO. *J. Phys. Chem. Lett.* **2011**, *2*, 3045–3052.
- (118) Sarovar, M.; Cheng, Y. C.; Whaley, K. B. Environmental Correlation Effects on Excitation Energy Transfer in Photosynthetic Light Harvesting. *Phys. Rev. E* **2011**, *83*, 011906.
- (119) Schulze, J.; Shibl, M. F.; Al-Marri, M. J.; Kühn, O. Multi-layer multi-configuration time-dependent Hartree (ML-MCTDH) approach to the correlated exciton-vibrational dynamics in the FMO complex. *J. Chem. Phys.* **2016**, *144*, 185101.

- (120) Engel, G. S.; Calhoun, T. R.; Read, E. L.; Ahn, T.-K.; Mancal, T.; Cheng, Y.-C.; Blankenship, R. E.; Fleming, G. R. Evidence for wavelike energy transfer through quantum coherence in photosynthetic systems. *Nature* **2007**, *446*, 782–786.
- (121) Scholes, G. D.; Fleming, G. R.; Chen, L. X.; Aspuru-Guzi, A.; Buchleitner, A.; Coker, D. F.; Engel, G. S.; van Grondelle, R.; Ishizaki, A.; Jonas, D. M.; Lundeen, J. S.; McCusker, J. K.; Mukamel, S.; Ogilvie, J. P.; Olaya-Castro, A.; Ratner, M. A.; Spano, F. C.; Whaley, K. B.; Zhu, X. Using coherence to enhance function in chemical and biophysical systems. *Nature* **2017**, *543*, 647–656.
- (122) Zhu, J.; Kais, S.; Rebentrost, P.; Aspuru-Guzik, A. Modified Scaled Hierarchical Equation of Motion Approach for the Study of Quantum Coherence in Photosynthetic Complexes. *J. Phys. Chem. B* **2011**, *115*, 1531–1537.
- (123) Jang, S.; Cao, J.; Silbey, R. J. Fourth-order quantum master equation and its Markovian bath limit. *J. Chem. Phys.* **2002**, *116*, 2705–2717.
- (124) Mavros, M. G.; Van Voorhis, T. Resummed memory kernels in generalized system-bath master equations. *J. Chem. Phys.* **2014**, *141*, 054112.
- (125) Xu, M.; Yan, Y.; Liu, Y.; Shi, Q. Convergence of high order memory kernels in the Nakajima-Zwanzig generalized master equation and rate constants: Case study of the spin-boson model. *J. Chem. Phys.* **2018**, *148*, 164101.
- (126) Marcus, R. A. On the Theory of Oxidation-Reduction Involving Electron Transfer. *J. Chem. Phys.* **1956**, *24*, 966–978.
- (127) Marcus, R. A.; Sutin, N. Electron transfers in chemistry and biology. *Biochim. Biophys. Acta* **1985**, *811*, 265.
- (128) Marcus, R. A. Electron Transfer Reactions in Chemistry. Theory and Experiment. *Rev. Mod. Phys.* **1993**, *65*, 599–610.

- (129) Javadi-Abhari, A.; Treinish, M.; Krsulich, K.; Wood, C. J.; Lishman, J.; Gacon, J.; Martiel, S.; Nation, P. D.; Bishop, L. S.; Cross, A. W.; Johnson, B. R.; Gambetta, J. M. Quantum computing with Qiskit. 2024.
- (130) Ishizaki, A.; Fleming, G. R. On the Adequacy of the Redfield Equation and Related Approaches to the Study of Quantum Dynamics in Electronic Energy Transfer. *J. Chem. Phys.* **2009**, *130*, 234110.
- (131) Khodjasteh, K.; Lidar, D. A. Fault-Tolerant Quantum Dynamical Decoupling. *Phys. Rev. Lett.* **2005**, *95*, 180501.
- (132) Uhrig, G. S. Keeping a Quantum Bit Alive by Optimized  $\pi$ -Pulse Sequences. *Phys. Rev. Lett.* **2007**, *98*, 100504.
- (133) Pokharel, B.; Anand, N.; Fortman, B.; Lidar, D. A. Demonstration of Fidelity Improvement Using Dynamical Decoupling with Superconducting Qubits. *Phys. Rev. Lett.* **2018**, *121*, 220502.
- (134) Ezzell, N.; Pokharel, B.; Tewala, L.; Quiroz, G.; Lidar, D. A. Dynamical decoupling for superconducting qubits: A performance survey. *Phys. Rev. Appl.* **2023**, *20*, 064027.
- (135) Devitt, S. J.; Munro, W. J.; Nemoto, K. Quantum error correction for beginners. *Rep. Prog. Phys.* **2013**, *76*, 076001.
- (136) Gottesman, D. An introduction to quantum error correction and fault-tolerant quantum computation. Quantum information science and its contributions to mathematics, Proceedings of Symposia in Applied Mathematics. 2010; pp 13–58.
- (137) Convy, I.; Liao, H.; Zhang, S.; Patel, S.; Livingston, W. P.; Nguyen, H. N.; Siddiqi, I.; Whaley, K. B. Machine learning for continuous quantum error correction on superconducting qubits. *New. J. Phys.* **2022**, *24*, 063019.

- (138) Andreasson, P.; Johansson, J.; Liljestrand, S.; Granath, M. Quantum error correction for the toric code using deep reinforcement learning. *Quantum* **2019**, *3*, 183.
- (139) Strathearn, A.; Kirton, P.; Kilda, D.; Lovett, B. W. Efficient non-Markovian quantum dynamics using time-evolving matrix product operators. *Nat. Commun.* **2018**, *9*, 3322.
- (140) Jørgensen, M. R.; Pollock, F. A. Exploiting the Causal Tensor Network Structure of Quantum Processes to Efficiently Simulate Non-Markovian Path Integrals. *Phys. Rev. Lett.* **2019**, *123*, 240602.
- (141) Richter, M.; Hughes, S. Enhanced TEMPO Algorithm for Quantum Path Integrals with Off-Diagonal System-Bath Coupling: Applications to Photonic Quantum Networks. *Phys. Rev. Lett.* **2022**, *128*, 167403.
- (142) Cabral, D. G.; Khazaei, P.; Allen, B. C.; Videla, P. E.; Schäfer, M.; Cortiñas, R. G.; de Albornoz, A. C. C.; Chávez-Carlos, J.; Santos, L. F.; Geva, E.; others A Roadmap for Simulating Chemical Dynamics on a Parametrically Driven Bosonic Quantum Device. *arXiv preprint arXiv:2409.13114* **2024**,
- (143) Dutta, R.; Cabral, D. G. A.; Lyu, N.; Vu, N. P.; Wang, Y.; Allen, B.; Dan, X.; Cortiñas, R. G.; Khazaei, P.; Schäfer, M.; Albornoz, A. C. C. d.; Smart, S. E.; Nie, S.; Devoret, M. H.; Mazziotti, D. A.; Narang, P.; Wang, C.; Whitfield, J. D.; Wilson, A. K.; Hendrickson, H. P.; Lidar, D. A.; Pérez-Bernal, F.; Santos, L. F.; Kais, S.; Geva, E.; Batista, V. S. Simulating Chemistry on Bosonic Quantum Devices. *J. Chem. Theory Comput.* **2024**, *20*, 6426–6441.
- (144) Crane, E.; Smith, K. C.; Tomesh, T.; Eickbusch, A.; Martyn, J. M.; Kühn, S.; Funcke, L.; DeMarco, M. A.; Chuang, I. L.; Wiebe, N.; others Hybrid Oscillator-Qubit Quantum Processors: Simulating Fermions, Bosons, and Gauge Fields. *arXiv preprint arXiv:2409.03747* **2024**,

- (145) Liu, Y.; Singh, S.; Smith, K. C.; Crane, E.; Martyn, J. M.; Eickbusch, A.; Schuckert, A.; Li, R. D.; Sinanan-Singh, J.; Soley, M. B.; others Hybrid oscillator-qubit quantum processors: Instruction set architectures, abstract machine models, and applications. *arXiv preprint arXiv:2407.10381* **2024**,
- (146) Lyu, N.; Bergold, P.; Soley, M. B.; Wang, C.; Batista, V. S. Holographic Gaussian Boson Sampling with Matrix Product States on 3D cQED Processors. *J. Chem. Theory Comput.* **2024**, *20*, 6402–6413.

# Supporting Information: qHEOM: A Quantum Algorithm for Simulating Non-Markovian Quantum Dynamics Using the Hierarchical Equations of Motion

## Quantum circuits

In this section, we give examples of the quantum circuits used in the main text. All quantum circuits were compiled according to the topology of the corresponding IBM quantum computer, specifically the IBM Sherbrooke, with the basis gate set consisting of  $X$ ,  $\sqrt{X}$ ,  $R_z$ , and ECR gates. The compilation processes were executed using the Qiskit package.<sup>129</sup>

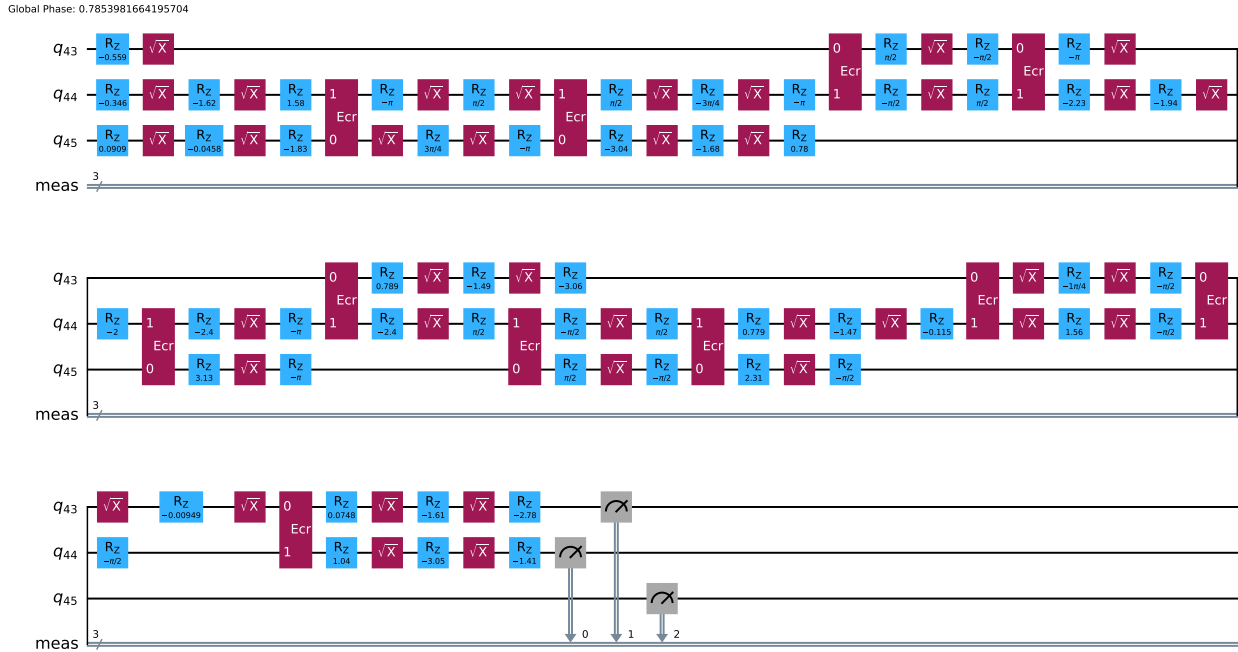


Figure 12: Quantum circuit for the molecular triad charge transfer model in the linear conformation, with the propagator at  $t = 2073.5$  fs. The projection subspace  $S = \{DD, DA, AD, AA\}$  corresponds to 3 qubits after dilation. The circuit depth is 60, with the following gate counts: 55  $R_z$  gates, 38  $\sqrt{X}$  gates, and 11 ECR gates.

Global Phase: 5.496607690133003

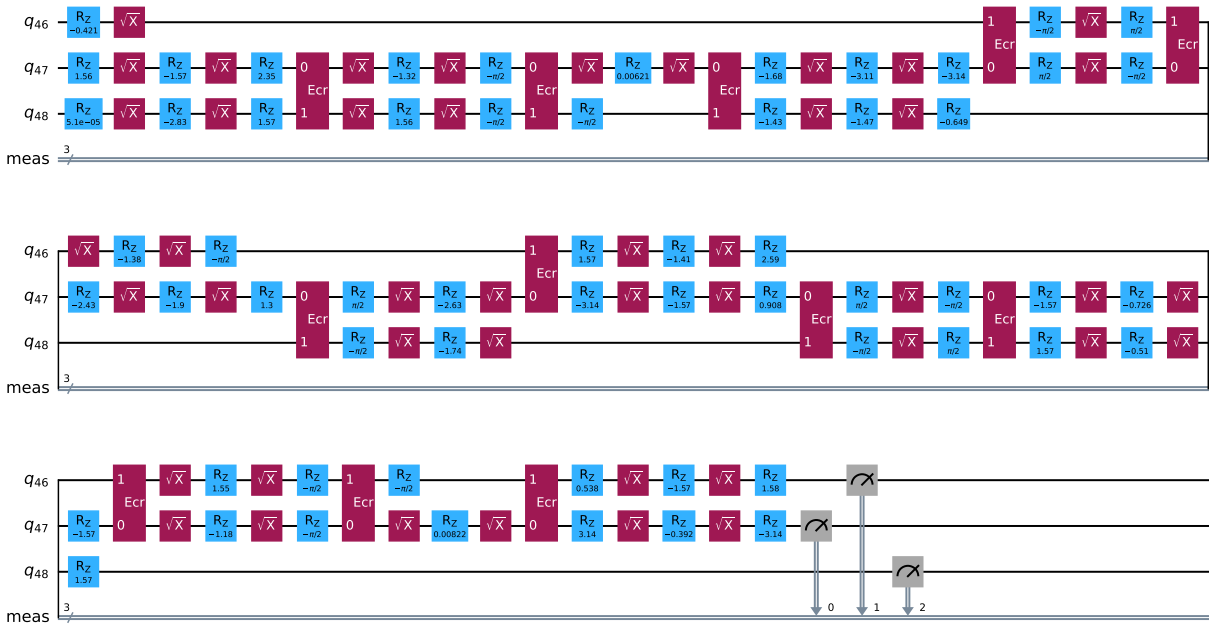


Figure 13: 3-qubit quantum circuit corresponding to the propagator at  $t = 612.0$  fs for the excitation energy transfer model in the FMO complex, the projection subspace  $S = \{11, 22, 33, 66\}$ . The circuit depth is 67, with 60  $R_z$  gates, 45  $\sqrt{X}$  gates, and 12 ECR gates.

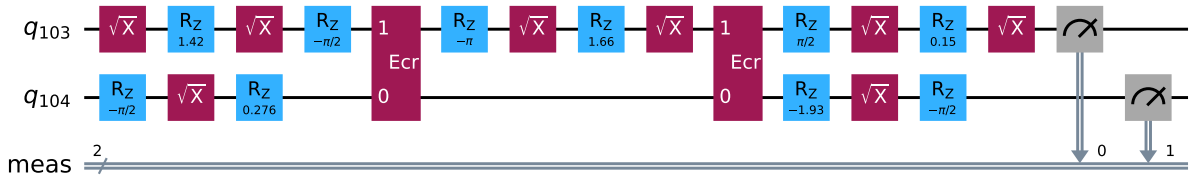


Figure 14: Quantum circuit for the 2-qubit linear conformation molecular triad charge transfer model (the projection subspace  $S = \{DD, AA\}$ ), corresponding to the propagator at  $t = 2073.5$  fs. The circuit depth is 15, with the following gate counts: 10  $R_z$  gates, 8  $\sqrt{X}$  gates, and 2 ECR gates.



Global Phase: 3.140390908474938

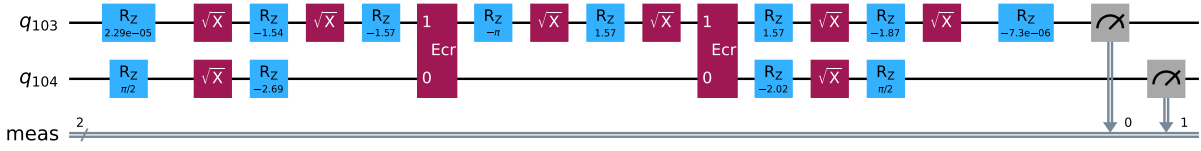


Figure 15: 2-qubit quantum circuit corresponding to the propagator at  $t = 612.0$  fs for the excitation energy transfer model in the FMO complex, with the projection subspace  $S = \{11, 22\}$ . The circuit depth is 17, with 12  $R_z$  gates, 8  $\sqrt{X}$  gates, and 2 ECR gates.

## Results without error mitigation

This section presents the NISQ results without error mitigation techniques for charge transfer in the molecular triad and energy transfer in the FMO complex.

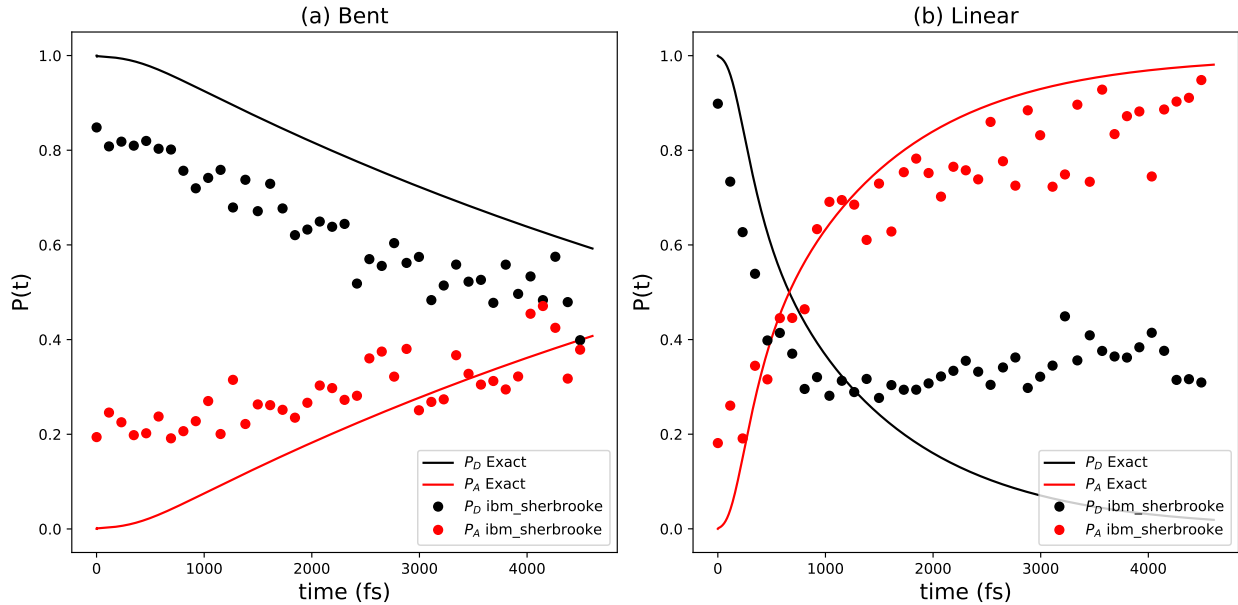


Figure 16: Population dynamics of the molecular triad without error mitigation: (a) Bent conformation, (b) linear conformation.  $P_D$  denotes the population in the  $\pi\pi^*$  (donor) state, while  $P_A$  denotes the population in the CT1 (acceptor) state. The solid lines represent the exact HEOM results, and the scatter points represent the quantum circuit results from the IBM Sherbrooke computer. The projection subspace  $S = \{DD, DA, AD, AA\}$ . Each time point is measured at 20000 shots.

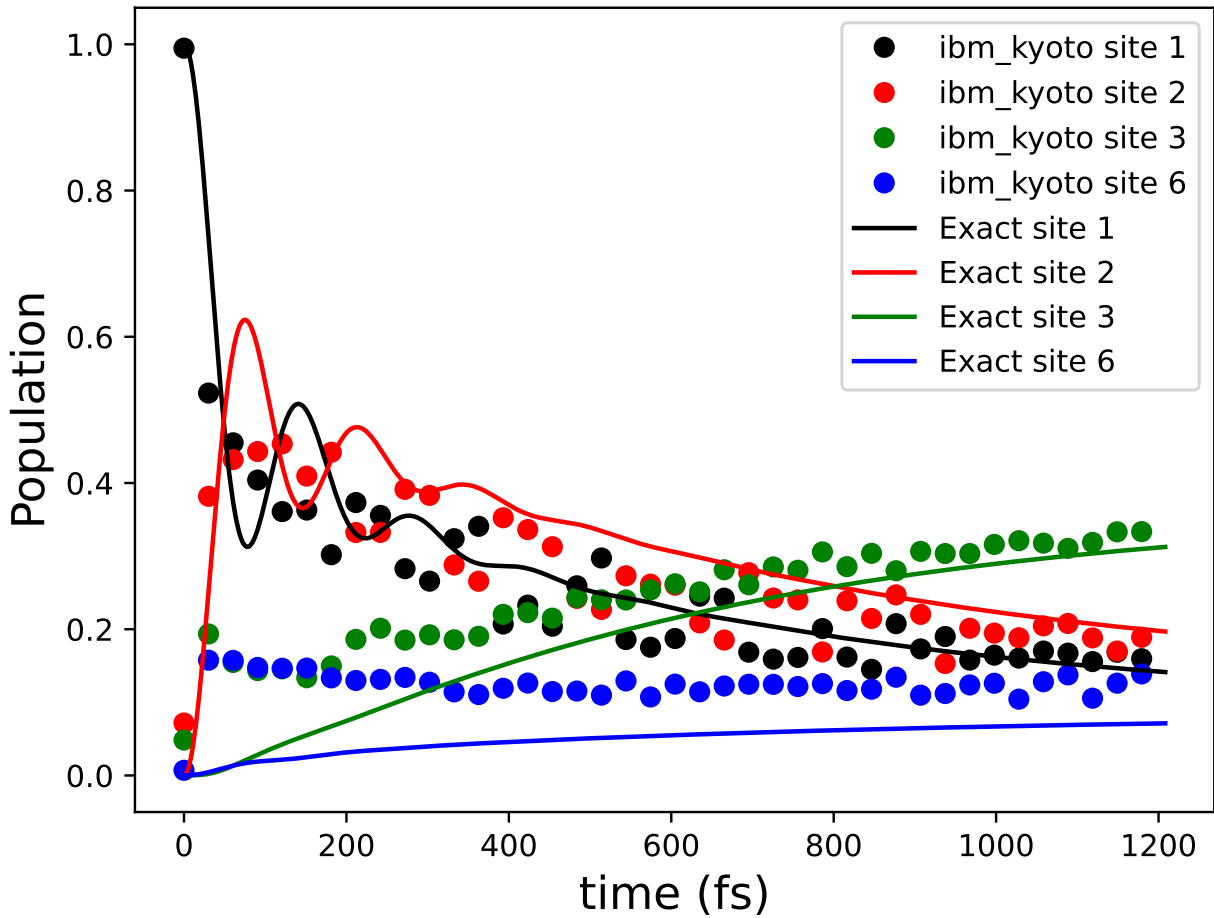


Figure 17: Population dynamics of the FMO complex without error mitigation. The solid lines represent the exact HEOM simulation results, and the scatter points represent the quantum circuit results from the IBM Kyoto quantum computer. The projection subspace  $S = \{11, 22, 33, 66\}$ . Each time point is measured at 20000 shots.